

## ESO Imaging Survey

### Hubble Deep Field South: Optical-Infrared Observations, Data Reduction and Photometry

L. da Costa<sup>1</sup>, M. Nonino<sup>1,2</sup>, R. Rengelink<sup>1</sup>, S. Zaggia<sup>1,3,4</sup>, C. Benoist<sup>1,5</sup>, T. Erben<sup>1,5</sup>, A. Wicenec<sup>1</sup>, M. Scodreggio<sup>1</sup>, L. F. Olsen<sup>1,6</sup>, D. Guarnieri<sup>7</sup>, E. Deul<sup>1,8</sup>, S. D'Odorico<sup>1</sup>, R. Hook<sup>9</sup>, A. Moorwood<sup>1</sup>, and R. Slijkhuis<sup>1</sup>

<sup>1</sup> European Southern Observatory, Karl-Schwarzschild-Str. 2, D-85748 Garching b. München, Germany

<sup>2</sup> Osservatorio Astronomico di Trieste, Via G.B. Tiepolo 11, I-31144 Trieste, Italy

<sup>3</sup> Dipartimento di Astronomia, Univ. di Padova, vicolo dell'Osservatorio 5, I-35125, Padova, Italy

<sup>4</sup> Osservatorio Astronomico di Capodimonte, via Moiariello 15, I-80131, Napoli, Italy

<sup>5</sup> Max-Planck Institut für Astrophysik, Postfach 1523 D-85748, Garching bei München, Germany

<sup>6</sup> Astronomisk Observatorium, Juliane Maries Vej 30, DK-2100 Copenhagen, Denmark

<sup>7</sup> Osservatorio Astronomico di Pino Torinese, Strada Osservatorio 20, I-10025 Torino, Italy

<sup>8</sup> Leiden Observatory, P.O. Box 9513, 2300 RA Leiden, The Netherlands

<sup>9</sup> Space Telescope – European Coordinating Facility, Karl-Schwarzschild-Str. 2, D-85748 Garching b. München, Germany

Received ; accepted

**Abstract.** This paper presents ground-based data obtained from deep optical and infrared observations of the HST Hubble Deep Field South (HDF-S) field carried out at the ESO 3.5 New Technology Telescope (NTT). These data were taken as part of the ESO Imaging Survey (EIS) program, a public survey coordinated by ESO and member states, in preparation for the first year of operation of the VLT. Deep CCD images are available for five optical passbands, reaching  $2\sigma$  limiting magnitudes of  $U_{AB} \sim 27.0$ ,  $B_{AB} \sim 26.5$ ,  $V_{AB} \sim 26$ ,  $R_{AB} \sim 26$ ,  $I_{AB} \sim 25$ , covering a region of  $\sim 25$  square arcmin, which includes the HST WFPC2 field. The infrared observations cover a total area of  $\sim 42$  square arcmin and include both the HST WFPC2 and STIS fields. The observations of the WFPC2 region were conducted in  $JHKs$  passbands, reaching  $J_{AB} \sim 25$ , and  $H_{AB}$  and  $K_{AB} \sim 24.0$ . Due to time constraints, the adjacent field, covering the STIS field, has been observed only in  $R$ ,  $I$  and  $JHKs$ , while no observations were conducted covering the NIC3 field. This paper describes the observations and data reduction. It also presents images of the surveyed region and lists the optical and infrared photometric parameters of the objects detected on the co-added images of each passband, as well as multicolor optical and infrared catalogs. These catalogs together with the astrometrically and photometrically calibrated co-added images are being made public world-wide and can be retrieved from the world-wide web (<http://www.eso.org/eis>).

**Key words:** catalogs – surveys – stars:general – galaxies:general – cosmology:observations

#### 1. Introduction

One of the main goals of the ESO Imaging Survey (EIS, Renzini & da Costa 1997) has been to carry out deep, multi-color observations in the optical and infrared passbands over a relatively large area ( $\sim 200$  square arcmin) to produce faint galaxy samples (EIS-DEEP). The primary objective is to use the color information to estimate photometric redshifts, and identify galaxies likely to be in the poorly sampled  $1 \lesssim z < 2$  redshift interval or Lyman-break candidates at  $z \gtrsim 2.5$ , all interesting targets for follow-up spectroscopic observations with the VLT.

Following the remarkable success of the HST observations of the Hubble Deep Field (HDF) in the North, the STScI has now completed a similar campaign in a second field, this time accessible from southern-hemisphere facilities. For HDF-S, the HST carried out simultaneous observations with three of its major instruments (WFPC2, STIS, and NICMOS) in parallel observing modes, leading to deep images of three separate fields. Another important difference relative to the original HDF is that instead of using an "undistinguished" field, the selected pointing for HDF-S was chosen to contain a QSO within the STIS field. Although this choice is interesting in many respects, the selected field is close to a very bright star as well as several to relatively bright stars, making it less than ideal for wide-angle, deep ground-based optical and near-infrared observations.

To reconcile the great interest generated by the HDF-S with the desire to conduct observations in a less crowded field, the EIS Working Group recommended the EIS-DEEP observations to be split into two sets: one set consisting of three adjacent fields, of about 25 square arcmin each, covering the WFPC2, STIS and NIC3 fields; and another set consisting of four adja-

**Table 1.** SUSI2 and SOFI Pointings

Field	$\alpha_{\text{susi2}}$	$\delta_{\text{susi2}}$	$\alpha_{\text{sofi}}$	$\delta_{\text{sofi}}$
HDF1	22:33:29.1	-60:33:50	22:33:32.5	-60:33:30
HDF2	22:32:42.4	-60:33:50	22:33:00.0	-60:33:30

cent fields, comprising a total area of 100 square arcmin. covering a region of very low HI column density at  $\alpha = 03^{\text{h}}32^{\text{m}}28^{\text{s}}$  and  $\delta = -27^{\circ}48'30''$ . This field is particularly interesting as deep imaging in X-ray of the region is planned with AXAF.

In the present paper the data from observations of the HDF-S field, conducted in five optical and three infrared passbands over the period August-November 1998, are reported. In section 2, the observations and data reduction are discussed, and co-added images for the different fields and passbands are presented. In section 3, the basic photometric parameters of sources detected in each passband are listed. In addition, optical, infrared and optical-infrared multicolor catalogs, based on detections in a combined reference image are presented. In section 4, a comparison of the data is made with other observations of the same field to evaluate the completeness and the accuracy of the magnitude measurements. Using both the single-band and multi-color catalogs the characteristics of the data are explored in section 5 where galaxy and star number counts as well as color-color diagrams are presented. Finally, a preliminary list of high- $z$  galaxy candidates is selected. A brief summary is presented in section 6.

## 2. Observations and Data Reduction

### 2.1. Observing Strategy

The original goal of the EIS-DEEP observations of the HDF-S fields was to observe three adjacent, and preferably contiguous, regions overlapping the WFPC2, STIS and the NIC3 fields both in optical and infrared. Therefore, the pointings of the optical and infrared cameras were chosen based on the relative separation of these fields and the physical characteristics of the cameras, thereby constraining the final sky coverage and the overlap between the optical and infrared observations.

The optical observations were carried out using the SUSI2 camera (D’Odorico *et al.* 1998) at the f/11 Nasmyth focus A of the New Technology Telescope (NTT). The camera consists of two thinned, anti-reflection coated,  $2k \times 4k$ ,  $15\mu\text{m}$  pixel EEV CCDs (ESO #45, and #46), with the long side aligned in the north-south direction, leading to a field of view of  $5.46 \times 5.46$  square arcmin. The pixel scale of the camera is 0.08 arcsec/pixel but the observations were carried out using a  $2 \times 2$  binning, yielding a scale of 0.16 arcsec per pixel. On the sky the gap separating the two CCDs corresponds to  $\sim 8$  arcsec. The observations were carried out in a dithered pattern, designed to minimize the lack of sensitivity at the center of the camera due to the gap. The dithering pattern adopted for SUSI2 consisted of eleven pointings, evenly distributed within a rectangular box 40 arcsec long in right ascension and 8 arcsec wide in decli-

**Table 2.** Summary of Optical Observations

Filter	$t_{\text{total}}$	$N_f$	seeing range	FWHM	$\mu_{\text{lim}}$
	(sec)		(arcsec)	(arcsec)	(mag arcsec $^{-2}$ )
<b>HDF1</b>					
<i>R</i>	5500	22	0.8-1.3	1.15	28.01
<i>I</i>	3600	6	1.3-1.5	1.50	26.86
<b>HDF2</b>					
<i>U</i>	17800	22	0.7-1.2	1.00	27.87
<i>B</i>	6600	22	0.7-1.2	0.84	28.88
<i>V</i>	12250	49	0.9-1.5	1.27	28.89
<i>R</i>	5500	22	0.8-1.3	1.05	28.01
<i>I</i>	8800	44	0.9-1.4	1.11	27.23

nation. The region where the sensitivity of the combined images is  $\gtrsim 70\%$  is considered below to be the effective size of the observations in a given passband. After the combination of the 11 pointings, this area includes the gap and a small region close to the outer edge of the frame, where the sensitivity drops to about 70% or  $\sim 0.25$  mag brighter than the limit reached in regions covered by all frames. The effective area covered by one SUSI2 observation is therefore  $5.20 \times 5.40$  square arcmin, corresponding to 94% of the SUSI2 field of view in a single exposure. Using the weight map computed by the EIS pipeline, a mask for each passband was created which accurately reflects the effective area. However, since there may be small relative shifts of the centers of the co-added images in different passbands, a master mask has also been created (the product of the individual band masks), to identify all the pixels that are above a minimum sensitivity ( $\gtrsim 70\%$ ) in all bands. Light streaks, associated with stars outside the field of view, have also been masked out. The final effective area used to trim all the co-added images is about  $5.3 \times 5.3$  square arcmin. All catalogs presented below have been compiled using objects extracted within this common area, except in the *U*-band, where an additional region was masked out to avoid the effects associated with the wings of a bright star in the field.

Since the size of the HST-WFPC2 field of view ( $\sim 158$  arcsec) is comparable to the short axis of one SUSI2 chip ( $\sim 164$  arcsec), the nominal center of the SUSI2 observations of the WFPC2 field was chosen so that the latter would lie within a single SUSI2 chip, with the center slightly shifted to the west to avoid as much as possible the lack of sensitivity due to the gap. The original idea was that the lack of sensitivity at the eastern edge of the chip, also affected by the dithering, would be compensated by exposures of the adjacent field covering the STIS field. Taking these constraints into consideration the reference pointings finally adopted for SUSI2 are listed in Table 1 for the two fields observed. To illustrate the geometry of the EIS observations of HDF-S, Figure 1 shows the co-added *R*-band image built from the images taken in the direction of the STIS and WFPC2 fields, hereafter referred to as HDF1 and HDF2. Also shown are the locations of the two SUSI2 chips when the centers listed in Table 1 are used. For comparison the approximate locations of the HST-WFPC2 and STIS fields are also dis-

This figure is available as fig1.jpg

**Fig. 1.** EIS-DEEP observations of the HDF-S. The image corresponds to the co-added *R*-band image, the only optical image currently available covering both the HST-WFPC2 and STIS fields, depicted in the figure. Also shown are the positions of the two SUSI2 chips (the paired rectangles) and the SOFI coverage (the large squares) at the nominal pointings listed in Table 1. The SUSI2 gap and the SOFI overlap can be clearly seen. For all images shown in this paper north is up and east to the left.

played. Complementing this information, Figure 2 shows a cut at fixed declination of the corresponding *R*-band weight-map, from which the variation of the response as a function of right ascension can be seen. Unfortunately, poor weather conditions early in the observing period limited the optical observations of the HDF1 (STIS) field to the *R*-band and about one-third of the desired exposure in *I*-band. This implies that the eastern-most edge of the WFPC2 field lies in the region, some 30 arcsec wide, where the sensitivity of the SUSI2 exposures drops sharply.

Infrared observations were obtained using the SOFI camera (Moorwood, Cuby & Lidman 1998) also at the NTT. SOFI is equipped with a Rockwell 1024<sup>2</sup> detector that, when used together with its large field objective, provides images with a pixel scale of 0.29 arcsec, and a field of view of about  $4.9 \times 4.9$  square arcmin. Because of the somewhat smaller field of view of SOFI, the infrared pointings were chosen to have the fully sampled pixels (discarding the edges due to the jitter pattern) overlapping and covering both STIS and WFPC2. This led to the centers listed in Table 1 and the coverage illustrated in Figure 1. The final areas covered by SOFI are 21.3 and 21.5 square arcmin in HDF1 and HDF2, respectively, with some overlap.

The infrared observations were jittered relative to the centers given above. The procedure consists of a series of short exposures with small position offsets from the target position. This strategy is used to deal with a background that (i) will saturate the chip in a short time ( $\sim 1$  minute), and (ii) varies on short time-scales. The aim is to remove the sky signal in each

pixel of the image, using observations of the same pixel as it points at different parts of the sky. The jitter strategy has been implemented as a standard observing template (*AutoJitter*) for the SOFI instrument. Using this template, offsets are generated randomly within a square box of a specified size  $s$ , chosen to be  $s = 45$  arcsec, approximately 10% of the SOFI detector field of view. These offsets are constrained so that all distances between pointings, in a series of 15 consecutive pointings are larger than 9 arcsec. Individual observations comprised sixty one-minute exposures with offsets generated by the *AutoJitter* template. Each exposure consisted of the average of six ten-second sub-exposures.

## 2.2. Optical Data

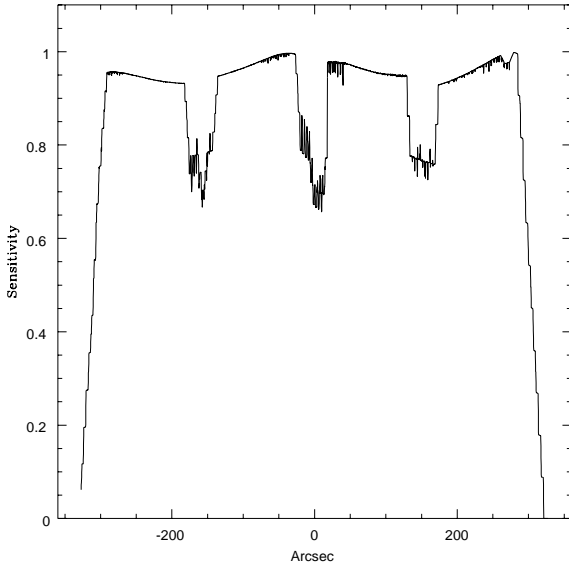
The optical observations were carried out in the period August–November 1998, using broad-band *UBVRI* filters (ESO # 810, 811, 812, 813, and 814, see SUSI2 web page). A total of 12 nights were allocated for optical EIS-DEEP observations of the HDF-S and AXAF fields. However, because of poor weather conditions it was not possible to complete the program as originally envisioned. While the optical observations of HDF2 (WFPC2) field are complete, only *R* and some *I*-band data are currently available for HDF1 (STIS) and no observations were made of the NIC3 field.

Table 2 summarizes the observations, listing for each field and passband the total integration time, the number of exposures, the range of seeing as measured on individual exposures,



This figure is available as fig3.jpg

**Fig. 3.** Final HDF2 co-added image for each of the optical passbands (from left to right, top to bottom: U, B, V, R, and I). In the red passbands one sees the light streaks from bright stars outside the field and in the blue ( $U$ ) from the bright star in the upper right (northwest) corner of the images.



**Fig. 2.** Cut across the normalized weight map of the fully co-added SUSI2 *R*-band image shown in Figure 1. The figure shows the variation of the sensitivity across the image along the right ascension direction. Note how the dithering fills the gap between the chips and between the pointings.

the full-width at half-maximum (FWHM) of the point spread function (PSF) in the final co-added image, and the estimated  $1\sigma$  limiting isophote within a 1 square arcsec area. While most of the observations were conducted in photometric nights with relatively good seeing, data were also taken in nights when the transparency and seeing varied considerably. Single exposures ranged from 800 sec (*U*) to 200 sec (*I*).

Landolt standards taken from Landolt (1992) were observed during all clear nights and in all passbands used, thus allowing an accurate determination of the photometric zero-point, extinction and color terms. Independent solutions were found for each run typically using some 50 standard star measurements. A total of 9 nights were deemed photometric and frames in all passbands are available in these nights, thus allowing for a suitable absolute calibration of the observations. The photometric calibration was done independently for the two chips of the camera. Magnitudes for Landolt stars were obtained using an aperture 14 arcsec in diameter. Comparison of the listed magnitudes of the Landolt standards with the derived photometric solutions yields the following estimates for the accuracy of the zero-points:  $\pm 0.1$  mag in *U*;  $\pm 0.03$  mag in *B*;  $\pm 0.03$  mag in *V*;  $\pm 0.02$  mag in *R*; and  $\pm 0.05$  mag in *I*. These results apply to both chips, with the relative zero-point difference between the chips being smaller than their estimated errors. Relative to the Johnson-Cousins (JC) the following color terms have been computed:

$$\begin{aligned} (U_{JC} - U_{EIS}) &= 0.14(\pm 0.06) \times (U - V)_{JC}, \\ (B_{JC} - B_{EIS}) &= 0.14(\pm 0.02) \times (B - V)_{JC}, \\ (V_{JC} - V_{EIS}) &= 0.0(\pm 0.01) \times (B - V)_{JC}, \\ (R_{JC} - R_{EIS}) &= -0.04(\pm 0.01) \times (V - R)_{JC}, \\ (I_{JC} - I_{EIS}) &= 0.03(\pm 0.02) \times (V - I)_{JC}, \end{aligned}$$

The magnitudes were also corrected for galactic absorption, using  $E(B - V) = 0.027$  as derived from Schlegel, Finkbeiner & Davis (1998), yielding  $A_U = 0.14$  mag,  $A_B = 0.08$  mag,  $A_V = 0.07$  mag,  $A_R = 0.05$  mag and  $A_I = 0.04$  mag. To facilitate the comparison with the HDF data and other authors, below all magnitudes given below, unless otherwise specified, have been converted to the *AB* system using the following relations:  $U_{AB} = U + 0.82$ ;  $B_{AB} = B - 0.06$ ;  $V_{AB} = V$ ;  $R_{AB} = R + 0.17$ ; and  $I_{AB} = I + 0.42$ .

A total of 564 standard stars and 226 science frames were reduced using standard IRAF tasks. For each frame a pre-scan correction was applied, using the pre-scan region associated to each chip, and the frames trimmed. A master bias for each run was created by median combining all bias frames and applying a  $3\text{-}\sigma$  clipping. The same procedure was adopted for the dome flats and sky-flats. All frames were corrected using the dome flat and an illumination correction based on the sky-flats. For the red passbands, in particular *I*, the images exhibit significant fringing. To partly remove the observed low-level pattern ( $\lesssim 5\%$ ) background maps were produced using SExtractor and were combined to create a superflat. The frames were then flat-field corrected using this superflat and each image was input to the IRAF *mkfringecor* task. The output fringe images were then combined into a master fringe frame. Finally, the master fringe frame was subtracted from the science frames. It should be noted that this procedure may result in the loss of faint objects. However, visual inspection of the fringe corrected images shows that the improvement of the images outweighs the loss of faint objects.

After all these corrections were applied, several hot pixels were still visible in the individual *U* and *B*-band exposures, especially in the CCD #46. While some were isolated pixels, others were clustered in four different regions forming complex patterns. These patterns were clearly visible after the images in a given band were co-added, leading to a significant number of spurious detections. To minimize their effect, a suitable mask was created and used in the co-addition. To create this mask the following procedure was adopted. All images in *U* and *B* were median-combined and a high count threshold was set so that only the hot pixels were visible, thereby allowing them to be masked out. Finally, after the frames were corrected for all instrumental effects, an eye-inspection was carried out to mask out other features such as satellite tracks and reflection spikes associated with two relatively bright stars outside and one inside the field covering the WFPC2 camera.

### 2.3. Infrared Data

Infrared observations in the *JHKs* bands, for which a total of 10 nights were allocated, were obtained during the same period as the optical data. Total integration times, the number of frames,

**Table 3.** Summary of Infrared Observations

Filter	$t_{total}$ (sec)	$N_f$	seeing range (arcsec)	FWHM (arcsec)	$\mu_{lim}$ (mag arcsec $^{-2}$ )
HDF1					
<i>J</i>	10800	180	1.3-1.4	1.37	25.37
<i>H</i>	3600	60	0.9-1.0	0.91	23.78
<i>Ks</i>	10800	180	0.9-1.0	0.90	23.83
HDF2					
<i>J</i>	10800	180	0.9-1.0	0.90	25.94
<i>H</i>	7200	120	0.8-0.9	0.85	24.06
<i>Ks</i>	18000	300	0.7-1.2	0.96	24.22

the seeing range, the FWHM measured on the co-added images, and the estimated  $1\sigma$  limiting isophote within one square arcsec are given in Table 3.

During all nights infrared standards taken from Persson (1997) were observed. From the photometric solutions the errors in the absolute photometric zero-points are found to be:  $\pm 0.1$  mag in *J*;  $\pm 0.05$  mag in *H*; and  $\pm 0.1$  mag in *Ks* for HDF1; and  $\pm 0.05$  mag in *J*;  $\pm 0.05$  mag in *H*; and  $\pm 0.05$  mag in *Ks* for HDF2. These magnitudes were also converted to the *AB* system, using:  $J_{AB} = J + 0.89$ ;  $H_{AB} = H + 1.38$ ; and  $K_{AB} = Ks + 1.86$ .

The reduction of SOFI imaging data which include a total of 545 standard stars and 1020 science frames requires one major step particular to infrared data. This step uses the individual exposures to filter and subtract the sky-background. Because the telescope pointing error introduces an uncertainty in the image offsets, the exact offsets have to be determined, so that all exposures can be shifted and added. All these steps have been incorporated in the program *jitter*, from the astronomical data-reduction package *eclipse*, written by N. Devillard (Devillard, 1998).

The background filtering and subtraction uses the algorithm *sky-combine* in the *jitter* program. This algorithm finds, for each pixel in an exposure, the 14 pixel values for the 7 observations prior to and subsequent to that observation. Each of the 15 pixel values (including the current pixel) is divided by the median sky for the exposure it belongs to. The two smallest and largest values are rejected from the scaled array of 15 pixels, and the remaining values are averaged and subtracted from the central pixel. After sky subtraction, the image offsets between each exposure and the first exposure, which has by definition a zero offset from the target, are determined. In the first exposure a region of interest is defined by choosing an area of  $25 \times 25$  pixels around a bright peak near the center of the image. For each subsequent image the telescope offset is determined by cross-correlating the region of interest in the first image with the equivalent region in the offsetted image. Finally, all images are re-sampled into an output image for which the projection is equal to the projection of the first image, using a hyperbolic tangent kernel. After all exposures have been re-sampled, they are averaged to produce one final de-jittered image. The *jitter*-program also takes care of bias subtraction, flatfielding and in-

terpolation of bad-pixels prior to sky subtraction, as well as cleaning of columns that are affected by “bleeding” from very bright stars in the combined image after the shift and add procedure. Because of the jitter pattern the sensitivity of the combined image falls off at the edges. Therefore, the effective area is  $4.6 \times 4.6$  square arcmin.

#### 2.4. Processing

After removing the instrumental signatures, both optical and infrared images were input to the EIS pipeline for astrometric calibration using the USNO-A V1.0 catalog as reference. In the case of SUSI2, independent astrometric solutions were found for the two chips. Before the astrometric calibration, images were processed by SExtractor using a high detection threshold to measure the size of the PSF of each frame, to create weight maps for co-addition and to flag cosmic rays and defects using the Artificial Retina algorithm described in Nonino *et al.* (1998). These features were incorporated into the mask created earlier based on the hot pixels, bad columns and diffraction spikes. Images in the same passband were then co-added using the “drizzle” method, originally created to handle HST images (Fruchter & Hook 1998), at the same resolution as the original images. In the process of co-addition, images taken in photometric nights were used as reference and all other images were corrected to have the same instrumental magnitudes after extinction correction. Finally, the absolute zero-point was determined and stored in the header of the co-added image.

The resulting co-added optical images for the HDF2 field in each passband are shown in Figure 3. These are the full images without any trimming of the edges where the dithering pattern can be seen. Note that the *R*-band image of HDF1, covering the HST-STIS field shows some stray light and the one hour *I*-band data have not yet been fully reduced. Once completed they will immediately be made publicly available. From Figure 3 one can immediately see why this region is not appropriate for ground-based deep imaging. In all passbands the influence of the bright star on the upper right (northwest) can be clearly seen. In *U* it shows as a bright halo which is not appropriately modeled by the object detection algorithm, leading to an increase in the number of detections in this region. The effects of other stars just outside the field of view are also clearly seen in the top part of the images in all in bands, becoming particularly strong in the red passbands. Unfortunately, these stars could not be avoided given the other constraints on the pointing (see Section 2). It is also worth emphasizing the superb performance of SUSI2 in the blue passbands. Even though the SUSI2 images cannot, of course, match the resolution of WFPC2 the limiting magnitude is comparable to that achieved from space in 1/10 of the time. This can be seen in Figure 5 where a small region of the sky observed by the HST-WFPC2 and SUSI2 are compared. Note, however, that the response of the WFPC2 FW300 filter peaks further in the *UV*.

Similarly, co-added images were produced for the infrared observations for each band and pointing. However, since in this case there are observations of two adjacent fields, which



This figure is available as fig4.jpg

**Fig. 4.** Final co-added infrared images in the passbands *J* (upper panel), *H* (middle panel) and *Ks* (lower panel). These observations cover both HST-WFPC2 and STIS fields. Note that the integration time in *H*-band is less than the others and that the *Ks* image over the WFPC2 field is considerably deeper. The images are about  $9.0 \times 4.8$  square arcmin.

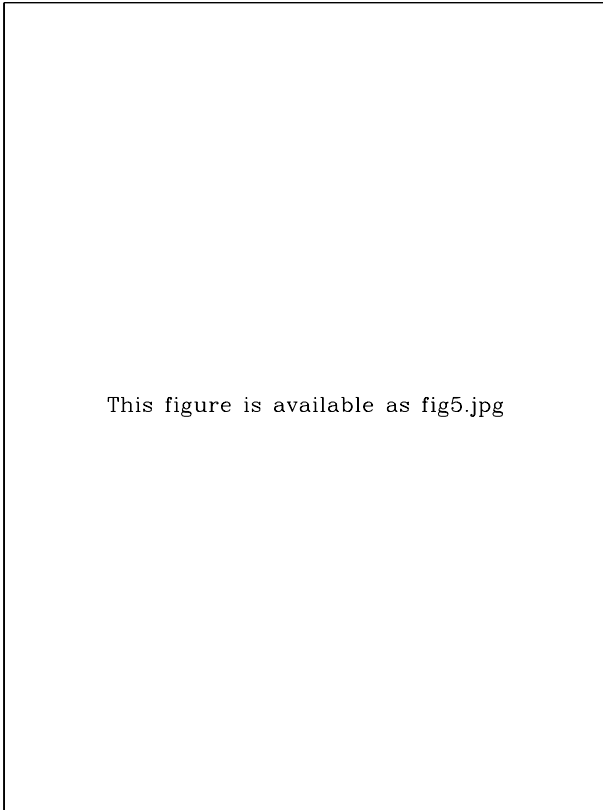


**Fig. 5.** Comparison between the  $U$ -band images from WFPC2 and SUSI2. While the resolution from space is unmatched, the detection limit is comparable even though the exposure time of the ground-based observations is 1/10 of that from HST. However, it should be noted that the passbands are different with that of WFPC2 located blueward compared to that of SUSI2.

overlap, additional co-added images, covering the WFPC2 and STIS fields, have been produced for each of the available passbands. These are shown in Figure 4. Note that the depth of the images may vary because of the different integration times in different fields. These infrared data which offer a unique complement to the HST observations are being made public worldwide.

Figure 18 is a true-color image of the HDF2 field with the blue channel represented by the  $U+B$ -band images, the green channel by the  $V+R$ -band images, and the red channel by the  $I$ -band image. As expected the image is dominated by faint blue galaxies, however several examples of red objects, some of which possibly high- $z$  candidates can also be found.

In addition, in order to allow the production of multi-color catalogs based on a single reference frame for detection, a co-added image of the optical data matching the infrared images resolution has also been created. Figure 19 shows a true-color image of the HDF2 field with the blue channel represented by the  $U+B+V$ -band images, the green channel by the  $R+I$ -band

images, and the red channel by the  $J+H+Ks$ -band images. This color image covers an area of approximately  $2.5 \times 4.0$  square arcmin, corresponding to the SUSI2-SOFI overlap covering the HST WFPC2 field.

All the co-added images, including the weights and masks, are public and may be requested from the URL "<http://www.eso.org/eis>".

### 3. Object Catalogs

The recent availability of large samples of high-quality, digital multi-band data, and improved techniques for assigning redshifts based on photometric data, have motivated great interest in the production of color catalogs of faint galaxies. Even though most methods use the same basic steps, they differ in the details on how to detect and measure magnitudes and colors as the detection threshold approaches the noise level. In general, when dealing with multi-band data, color catalogs can be produced either by the association of objects detected independently in each passband or by using some reference image to carry out the detection and to define apertures to be used for the subsequent measurement of magnitudes in each passband. Again the method of choice depends on the specific scientific goals, with each method susceptible to different bias. To avoid some of these issues single passband catalogs have been produced as well as examples of multicolor catalogs produced using a reference frame. A complete list of the catalogs currently available can be found on the EIS web page.

#### 3.1. Single Band Catalogs

Source extraction was performed using the SExtractor software (Bertin & Arnouts 1996). Detection was carried out separately using the co-added image of each passband and field. Star/galaxy classification was based on the stellarity-index given by SExtractor, which is approximately the probability of an object being a point-source. The main parameters in the detection are the smoothing kernel, taken to be a Gaussian with a FWHM comparable to that of the PSF as measured on the frame; the SExtractor detection threshold, taken to be 0.7; and the minimum number of pixels above the detection threshold, taken to be 10 and 7 pixels for the SUSI2 and SOFI images, respectively, because of the different pixel scales. As an illustration, the listing of the first 55 entries in the HDF2 source catalogs for  $U$  and  $Ks$ -bands are presented in Tables 4- 5. For each object the following parameters are given:

Column (1) - the entry number in the table (not to be misinterpreted as a unique reference to a specific object);

Columns (2) and (3): right ascension and declination (J2000.0);

Columns (4)-(9): total, isophotal (as measured by SExtractor) and aperture (2 arcsec in diameter) magnitudes and respective errors. The magnitudes have been corrected for extinction and converted to the  $AB$  system. The errors are the estimates from SExtractor, which only include the shot-noise on the measured source and background counts. These errors should be



**Table 4.** HDF-South. *U*-band Catalog of Sources in the HDF2 field.

#	$\alpha$	$\delta$	$m_{rot}$		$m_{iso}$		$m_{ap}$		$S/N$	$A$	$r_h$	$b/a$	PA	class	flags
(1)	(2)	(3)	(4)	(5)	(6)	(7)	(8)	(9)	(10)	(11)	(12)	(13)	(14)	(15)	(16)
1	22:32:18.74	-60:35:36.1	26.78	0.34	26.64	0.28	26.94	0.32	3.6	0.10	0.55	0.13	-2	0.35	3
2	22:32:18.82	-60:35:40.9	19.74	0.01	19.71	0.01	19.92	0.01	100.0	12.77	0.62	0.77	7	0.98	3
3	22:32:19.16	-60:34:30.5	26.71	0.34	26.71	0.34	26.81	0.42	2.9	0.05	0.38	0.90	1	0.35	1
4	22:32:19.18	-60:33:38.8	26.22	0.33	26.22	0.33	26.49	0.34	3.1	0.13	0.25	0.77	10	0.35	3
5	22:32:19.19	-60:34:50.0	24.96	0.23	24.82	0.13	25.26	0.14	7.6	0.67	0.64	0.96	71	0.64	1
6	22:32:19.19	-60:34:34.9	25.25	0.30	25.26	0.16	25.46	0.16	6.4	0.38	0.66	0.81	-6	0.34	1
7	22:32:19.26	-60:32:05.4	26.77	0.31	26.77	0.31	26.80	0.39	3.3	0.05	0.16	0.33	5	0.35	1
8	22:32:19.31	-60:32:31.0	25.87	0.23	25.87	0.23	25.93	0.23	4.3	0.13	0.54	0.71	7	0.65	3
9	22:32:19.32	-60:32:14.7	26.52	0.82	26.28	0.28	26.36	0.31	3.5	0.05	0.42	0.74	16	0.35	1
10	22:32:19.34	-60:32:41.8	26.38	0.34	26.38	0.34	26.85	0.48	3.0	0.10	0.13	0.94	-54	0.35	1
11	22:32:19.36	-60:32:35.6	23.17	0.06	23.15	0.06	24.17	0.08	18.1	4.68	1.21	0.90	4	0.00	3
12	22:32:19.39	-60:31:54.7	25.02	0.17	25.04	0.17	25.10	0.14	5.9	0.69	0.66	0.91	-83	0.47	1
13	22:32:19.46	-60:35:41.2	26.32	0.42	27.02	0.45	27.06	0.48	2.2	0.00	1.00	0.83	-24	0.35	3
14	22:32:19.47	-60:34:02.5	25.07	0.40	25.14	0.17	25.72	0.19	5.8	0.13	0.93	0.65	-23	0.35	3
15	22:32:19.47	-60:36:27.1	26.05	0.46	26.27	0.23	26.23	0.29	4.4	0.05	0.14	0.83	70	0.67	0
16	22:32:19.50	-60:35:06.9	26.78	0.33	26.78	0.33	26.80	0.40	3.0	0.03	0.51	0.70	-5	0.35	0
17	22:32:19.52	-60:35:03.1	26.35	0.28	26.35	0.28	26.37	0.28	3.6	0.03	0.42	0.93	-58	0.35	0
18	22:32:19.54	-60:34:17.6	26.00	0.21	26.00	0.21	26.14	0.24	4.7	0.10	0.37	0.95	-6	0.35	1
19	22:32:19.57	-60:34:58.9	26.66	0.39	26.66	0.39	26.94	0.45	2.5	0.03	0.81	0.54	14	0.35	1
20	22:32:19.57	-60:31:38.1	26.86	0.91	27.02	0.35	26.76	0.43	2.9	0.05	0.46	0.94	-76	0.35	0
21	22:32:19.59	-60:34:54.7	24.87	0.24	24.80	0.12	25.04	0.12	8.5	0.79	0.59	0.91	39	0.01	1
22	22:32:19.64	-60:32:17.5	26.41	0.87	26.64	0.32	26.77	0.43	3.2	0.03	0.71	0.78	-11	0.35	0
23	22:32:19.66	-60:33:01.6	24.15	0.13	24.13	0.08	24.45	0.09	12.3	1.77	0.68	0.91	-75	0.03	0
24	22:32:19.67	-60:34:20.8	25.74	0.58	25.34	0.16	25.73	0.18	6.2	0.28	0.56	0.67	-79	0.46	0
25	22:32:19.68	-60:32:50.6	25.31	0.40	24.75	0.12	25.23	0.14	8.5	0.69	0.63	0.61	88	0.49	1
26	22:32:19.72	-60:35:51.6	25.69	0.42	25.18	0.13	25.12	0.13	7.4	0.10	0.19	0.79	-83	0.64	0
27	22:32:19.73	-60:34:05.1	26.13	0.21	26.13	0.21	26.02	0.21	4.9	0.03	0.28	0.73	7	0.35	1
28	22:32:19.75	-60:33:23.7	26.92	0.49	26.92	0.49	26.75	0.37	2.0	0.00	0.16	0.86	7	0.35	0
29	22:32:19.77	-60:33:59.1	25.98	0.47	26.98	0.42	26.90	0.42	2.4	0.00	1.13	0.78	39	0.35	1
30	22:32:19.90	-60:34:25.2	25.31	0.34	25.64	0.18	25.76	0.18	5.7	0.23	0.75	0.85	65	0.34	0
31	22:32:19.90	-60:31:40.5	25.90	0.17	25.90	0.17	25.90	0.17	5.8	0.54	0.33	0.78	-61	0.50	3
32	22:32:20.01	-60:35:16.1	23.45	0.08	23.45	0.06	23.84	0.06	17.3	2.59	0.70	0.62	-47	0.25	2
33	22:32:20.06	-60:33:19.0	25.88	0.58	25.59	0.17	25.74	0.18	6.0	0.08	0.50	0.81	40	0.35	0
34	22:32:20.07	-60:34:09.9	24.24	0.13	24.14	0.08	24.61	0.09	12.6	1.54	0.72	0.95	-87	0.01	0
35	22:32:20.07	-60:33:10.9	25.23	0.51	26.20	0.34	27.33	0.63	2.9	0.03	2.03	0.74	61	0.35	3
36	22:32:20.10	-60:31:28.0	23.49	0.10	23.68	0.07	24.47	0.09	14.7	2.71	1.17	0.75	-14	0.00	0
37	22:32:20.10	-60:35:59.1	26.34	0.81	26.03	0.21	26.06	0.21	4.7	0.10	0.40	0.88	20	0.35	0
38	22:32:20.16	-60:32:43.0	27.27	0.42	27.27	0.42	26.54	0.32	2.4	0.03	0.16	0.83	59	0.35	0
39	22:32:20.16	-60:33:40.8	24.89	0.25	24.58	0.10	25.10	0.12	10.2	0.59	0.66	0.82	34	0.21	0
40	22:32:20.16	-60:32:05.5	24.55	0.11	24.55	0.11	25.14	0.13	8.9	0.74	0.28	0.72	-67	0.07	2
41	22:32:20.18	-60:35:27.8	26.15	0.24	26.15	0.24	26.23	0.25	4.2	0.05	0.16	0.91	-21	0.35	3
42	22:32:20.20	-60:35:30.5	26.37	0.83	25.66	0.18	26.00	0.21	5.6	0.18	0.44	0.75	44	0.35	3
43	22:32:20.20	-60:32:23.1	27.01	0.38	27.01	0.38	27.00	0.49	2.6	0.05	0.37	0.71	-38	0.35	0
44	22:32:20.25	-60:32:48.2	26.68	0.29	26.68	0.29	26.80	0.41	3.5	0.10	0.16	0.53	-30	0.63	1
45	22:32:20.26	-60:35:13.9	26.75	0.27	26.75	0.27	26.75	0.27	3.7	0.03	0.24	0.75	-45	0.35	3
46	22:32:20.26	-60:33:31.1	27.32	0.92	27.59	0.38	26.85	0.40	2.7	0.03	0.31	0.86	-47	0.35	0
47	22:32:20.29	-60:35:03.2	26.77	1.00	27.04	0.39	27.28	0.58	2.6	0.03	0.46	0.88	65	0.35	0
48	22:32:20.30	-60:34:31.1	25.82	0.19	25.82	0.19	25.98	0.20	5.2	0.05	0.36	0.71	-2	0.35	3
49	22:32:20.31	-60:36:33.4	26.87	0.77	27.24	0.40	27.04	0.48	2.5	0.00	0.44	0.82	75	0.35	1
50	22:32:20.32	-60:35:43.2	26.13	0.55	26.77	0.30	26.38	0.27	3.4	0.03	0.71	0.67	-48	0.35	0
51	22:32:20.33	-60:32:18.4	26.81	0.34	26.81	0.34	26.79	0.39	2.9	0.03	0.16	0.70	71	0.35	0
52	22:32:20.34	-60:31:40.8	22.30	0.04	22.31	0.04	23.30	0.05	28.4	9.27	1.18	0.87	58	0.00	2
53	22:32:20.35	-60:33:52.1	25.80	0.20	25.80	0.20	26.03	0.21	4.9	0.05	0.21	0.88	-22	0.35	0
54	22:32:20.37	-60:35:06.3	26.92	0.40	26.92	0.40	26.90	0.41	2.5	0.03	0.16	0.95	-32	0.35	0
55	22:32:20.43	-60:34:55.3	26.00	0.61	26.74	0.34	26.70	0.34	2.9	0.00	0.96	0.76	-28	0.35	0

considered as lower limits as they do not include the contribution from random or systematic errors in determining the mean sky level. However, as shown in Nonino *et al.* (1998) the SExtractor estimates are, in general, a good estimate of the error except, perhaps, at the very faint limit (see Figure 7). Also note

that the rms of the background in the co-added image is artificially small due to the effective small-scale smoothing introduced by the drizzling process. To correct for this effect the error estimated by SExtractor must be multiplied by a factor of 1.5. This correction has been taken into account in all the er-

**Table 5.** HDF-South. *Ks*-band Catalog of Sources in the HDF2 field.

#	$\alpha$	$\delta$	$m_{tot}$		$m_{iso}$		$m_{ap}$		$S/N$	$A$	$r_h$	$b/a$	PA	class	flags
(1)	(2)	(3)	(4)	(5)	(6)	(7)	(8)	(9)	(10)	(11)	(12)	(13)	(14)	(15)	(16)
1	22:32:41.24	-60:35:40.6	24.27	0.56	25.20	0.44	24.29	0.32	2.3	0.17	0.59	0.40	6	0.44	0
2	22:32:41.27	-60:33:59.8	22.89	0.25	24.20	0.29	23.67	0.20	3.4	0.50	1.03	0.57	8	0.36	2
3	22:32:41.27	-60:33:21.2	23.89	0.50	24.30	0.25	23.95	0.25	3.9	0.50	0.52	0.86	9	0.44	0
4	22:32:41.29	-60:33:16.6	22.35	0.15	23.99	0.24	24.05	0.27	4.2	0.33	2.24	0.81	45	0.46	0
5	22:32:41.38	-60:34:14.4	23.72	0.22	23.72	0.22	23.66	0.20	4.6	0.66	0.29	0.75	4	0.50	0
6	22:32:41.46	-60:32:07.8	23.35	0.32	24.51	0.29	23.91	0.24	3.5	0.33	0.90	0.75	80	0.19	0
7	22:32:41.48	-60:32:58.7	24.08	0.47	25.48	0.48	24.69	0.44	2.1	0.08	0.89	0.75	-53	0.35	0
8	22:32:41.53	-60:31:21.0	21.18	0.07	21.50	0.07	22.02	0.07	15.2	4.56	1.10	0.65	41	0.12	0
9	22:32:41.54	-60:35:15.7	19.47	0.02	19.46	0.02	20.17	0.03	44.6	15.84	0.95	0.83	-22	0.04	2
10	22:32:41.61	-60:33:45.1	24.57	0.82	25.11	0.42	24.61	0.41	2.4	0.00	0.55	0.56	76	0.35	0
11	22:32:41.66	-60:34:59.5	22.89	0.16	22.89	0.16	23.62	0.19	6.4	1.33	0.36	0.78	23	0.01	1
12	22:32:41.71	-60:34:25.4	18.91	0.02	18.88	0.02	19.23	0.02	62.9	15.51	0.63	0.94	56	0.98	0
13	22:32:41.84	-60:33:60.0	21.47	0.12	22.14	0.09	22.91	0.12	10.7	3.40	1.63	0.66	75	0.01	1
14	22:32:41.89	-60:33:21.1	23.62	0.70	23.17	0.17	23.60	0.19	5.8	0.83	0.64	0.82	-85	0.09	0
15	22:32:41.93	-60:34:54.8	21.79	0.13	21.59	0.07	21.98	0.07	15.2	4.48	0.64	0.94	-11	0.24	0
16	22:32:41.97	-60:35:21.5	22.91	0.42	22.56	0.12	23.13	0.14	8.4	1.58	0.70	0.70	-17	0.04	3
17	22:32:42.09	-60:31:36.2	24.48	0.35	24.48	0.35	24.62	0.41	2.9	0.25	0.29	0.71	26	0.47	0
18	22:32:42.10	-60:34:04.0	24.71	0.47	24.71	0.47	24.33	0.33	2.1	0.33	0.51	0.90	51	0.35	0
19	22:32:42.11	-60:34:08.6	23.07	0.16	23.07	0.16	23.60	0.19	6.4	1.08	0.22	0.92	6	0.13	0
20	22:32:42.15	-60:33:10.3	22.18	0.19	22.51	0.12	22.78	0.11	8.2	2.07	0.84	0.70	58	0.64	2
21	22:32:42.17	-60:33:34.6	22.16	0.17	23.33	0.17	23.41	0.17	5.7	1.08	2.30	0.84	-46	0.55	0
22	22:32:42.19	-60:34:46.1	23.26	0.37	22.74	0.12	22.82	0.11	8.1	1.91	0.39	1.00	-84	0.71	0
23	22:32:42.25	-60:32:55.1	24.17	0.53	24.95	0.34	24.62	0.42	2.9	0.41	0.54	0.62	-7	0.44	0
24	22:32:42.25	-60:32:17.6	23.52	1.00	23.19	0.22	23.91	0.24	4.5	0.91	0.80	0.56	70	0.36	2
25	22:32:42.31	-60:35:31.5	21.54	0.12	21.53	0.07	22.17	0.08	14.6	4.98	0.91	0.67	25	0.06	0
26	22:32:42.31	-60:32:42.3	22.62	0.28	23.21	0.17	23.84	0.23	5.9	0.66	1.30	0.90	78	0.39	3
27	22:32:42.31	-60:33:43.0	21.35	0.08	21.29	0.06	21.54	0.05	17.7	4.23	0.60	0.86	-14	0.97	0
28	22:32:42.39	-60:31:45.3	23.34	0.21	23.34	0.21	23.67	0.20	4.7	0.83	0.55	0.57	-67	0.13	2
29	22:32:42.41	-60:32:35.0	24.02	0.87	24.20	0.30	24.40	0.35	3.3	0.25	0.70	0.70	29	0.45	0
30	22:32:42.42	-60:34:24.6	23.62	0.53	24.86	0.44	24.92	0.53	2.3	0.00	1.43	0.64	63	0.35	1
31	22:32:42.48	-60:31:34.7	23.42	0.34	24.68	0.34	24.41	0.35	3.0	0.08	1.18	0.47	-36	0.35	0
32	22:32:42.49	-60:34:31.1	24.16	0.81	24.08	0.24	23.97	0.25	4.1	0.25	0.48	0.61	-62	0.36	0
33	22:32:42.66	-60:32:55.8	24.74	0.96	23.98	0.25	24.11	0.28	4.0	0.33	0.44	0.43	-17	0.35	0
34	22:32:42.67	-60:31:54.7	22.67	0.28	22.47	0.14	22.51	0.09	7.2	2.99	0.50	0.82	31	0.25	0
35	22:32:42.84	-60:33:13.4	22.96	0.36	23.44	0.21	23.42	0.17	4.9	1.08	0.77	0.69	51	0.26	0
36	22:32:42.88	-60:32:10.7	20.49	0.05	20.44	0.04	21.09	0.04	26.5	9.95	0.88	0.86	57	0.03	2
37	22:32:42.88	-60:34:05.2	23.42	0.65	23.30	0.18	23.72	0.21	5.5	1.00	0.77	0.49	-27	0.07	3
38	22:32:42.99	-60:32:41.8	18.75	0.01	18.75	0.02	19.32	0.02	65.8	20.98	0.85	0.73	-86	0.62	3
39	22:32:43.00	-60:31:16.7	23.70	0.85	22.87	0.14	23.24	0.15	7.2	1.82	0.44	0.55	78	0.01	0
40	22:32:43.00	-60:34:00.2	19.37	0.02	19.35	0.02	19.67	0.02	48.3	12.28	0.62	0.91	71	0.98	2
41	22:32:43.02	-60:34:08.0	23.56	0.21	23.56	0.21	24.03	0.26	4.8	0.50	0.29	0.42	-88	0.37	1
42	22:32:43.02	-60:34:21.1	21.86	0.14	22.12	0.09	22.55	0.10	11.0	3.15	0.94	0.82	42	0.24	1
43	22:32:43.08	-60:35:19.5	24.21	0.73	24.77	0.42	24.45	0.36	2.4	0.25	0.51	0.73	-31	0.38	0
44	22:32:43.09	-60:34:49.4	22.27	0.18	22.68	0.12	22.86	0.12	8.4	1.99	0.83	0.88	-69	0.30	0
45	22:32:43.11	-60:33:39.6	24.51	0.37	24.51	0.37	24.62	0.41	2.7	0.33	0.29	0.88	-3	0.36	0
46	22:32:43.21	-60:31:33.5	23.30	0.23	23.30	0.23	24.10	0.28	4.4	1.08	0.29	0.60	2	0.27	0
47	22:32:43.32	-60:32:37.4	22.70	0.29	23.19	0.16	23.39	0.17	6.2	1.00	0.95	0.71	-56	0.55	3
48	22:32:43.33	-60:33:04.2	23.00	0.14	23.00	0.14	23.22	0.15	7.3	1.24	0.29	0.57	-43	0.02	0
49	22:32:43.37	-60:35:45.1	24.70	0.39	24.70	0.39	24.54	0.39	2.5	0.08	0.29	0.65	19	0.35	0
50	22:32:43.37	-60:31:43.1	24.90	0.40	24.90	0.40	24.50	0.38	2.5	0.08	0.31	0.60	71	0.35	0
51	22:32:43.47	-60:34:41.9	18.00	0.01	18.00	0.01	18.93	0.02	94.3	36.33	1.14	0.53	-77	0.09	0
52	22:32:43.51	-60:33:51.1	19.66	0.02	19.67	0.02	20.07	0.03	41.7	11.78	0.69	0.98	-81	0.97	3
53	22:32:43.54	-60:35:21.3	24.11	0.26	24.11	0.26	24.02	0.26	3.9	0.50	0.12	0.45	72	0.05	0
54	22:32:43.56	-60:32:34.9	20.44	0.03	20.48	0.03	20.76	0.04	29.3	6.30	0.67	0.80	54	0.98	3
55	22:32:43.61	-60:35:14.1	24.45	0.27	24.45	0.27	24.02	0.26	3.7	0.41	0.29	0.67	-63	0.35	0

rors listed in all the object catalogs. Only objects detected with signal to noise  $S/N \geq 2$  (based on the isophotal magnitude) are included. Note that for faint objects it may occur that the total and aperture magnitudes have large errors. For those with mag-

nitude errors above 1 mag these magnitudes are replaced with the isophotal magnitude;

Column (10): an estimate of the  $S/N$  of the detection, using the errors estimated above for the isophotal magnitude;

**Table 6.** HDF-South. Multi-Color Optical Catalog from the  $\chi^2$  image in the HDF2 field.

#	$\alpha$	$\delta$	$m_U$	$m_B$	$m_V$	$m_R$	$m_I$	$A$										
(1)	(2)	(3)	(4)	(5)	(6)	(7)	(8)	(9)	(10)	(11)	(12)	(13)	(14)	(15)	(16)	(17)	(18)	(19)
1	22:32:18.74	-60:35:36.1	26.94	0.32	0.35	26.67	0.17	0.36	26.05	0.09	0.58	25.87	0.12	0.35	25.24	0.10	0.39	0.97
2	22:32:18.75	-60:35:23.9	99.99	9.99	0.35	99.99	9.99	0.35	28.51	0.97	0.35	26.36	0.31	0.35	27.15	0.81	0.35	0.56
3	22:32:18.82	-60:35:40.9	19.71	0.01	0.98	18.74	0.00	1.00	18.30	0.00	1.00	18.21	0.00	0.98	18.12	0.00	0.98	52.22
4	22:32:18.93	-60:35:55.6	99.99	9.99	0.35	99.99	9.99	0.35	99.99	9.99	0.35	99.99	9.99	0.35	26.67	0.66	0.35	0.84
5	22:32:18.96	-60:35:59.7	27.30	0.64	0.35	27.06	0.40	0.35	26.22	0.16	0.35	25.89	0.24	0.35	26.97	0.85	0.35	0.87
6	22:32:18.99	-60:35:14.4	27.41	0.70	0.35	25.76	0.13	0.35	24.85	0.06	0.61	24.38	0.06	0.40	23.98	0.06	0.48	5.68
7	22:32:19.00	-60:34:31.9	27.41	0.61	0.35	27.39	0.45	0.35	27.07	0.29	0.35	27.40	0.80	0.35	26.54	0.50	0.35	0.74
8	22:32:19.02	-60:34:21.3	99.99	9.99	0.35	27.04	0.33	0.35	27.00	0.27	0.35	26.61	0.39	0.35	26.09	0.33	0.35	1.05
9	22:32:19.02	-60:34:53.5	27.30	0.63	0.35	26.02	0.16	0.37	25.23	0.08	0.05	24.46	0.07	0.09	23.80	0.06	0.64	4.04
10	22:32:19.03	-60:33:51.0	99.99	9.99	0.35	99.99	9.99	0.35	27.00	0.25	0.35	99.99	9.99	0.35	99.99	9.99	0.35	1.28
11	22:32:19.05	-60:33:37.3	99.99	9.99	0.35	28.14	0.58	0.35	27.44	0.27	0.35	26.75	0.30	0.35	25.96	0.21	0.35	0.87
12	22:32:19.16	-60:34:30.5	26.81	0.42	0.35	26.36	0.21	0.35	26.13	0.15	0.35	26.08	0.29	0.35	25.99	0.35	0.35	2.59
13	22:32:19.17	-60:35:09.6	99.99	9.99	0.35	26.57	0.25	0.35	26.44	0.19	0.35	26.10	0.29	0.35	26.08	0.38	0.35	2.33
14	22:32:19.18	-60:33:38.8	26.49	0.34	0.35	25.92	0.15	0.31	24.96	0.06	0.10	24.34	0.07	0.21	24.05	0.07	0.42	5.89
15	22:32:19.19	-60:34:50.0	25.26	0.14	0.64	24.90	0.07	0.02	24.59	0.05	0.39	24.14	0.05	0.01	23.70	0.05	0.57	9.37
16	22:32:19.19	-60:34:44.0	99.99	9.99	0.35	26.87	0.33	0.35	27.13	0.34	0.35	26.48	0.41	0.35	26.56	0.59	0.35	0.46
17	22:32:19.19	-60:34:34.9	25.46	0.16	0.34	25.24	0.09	0.01	25.30	0.08	0.07	25.52	0.17	0.35	25.12	0.16	0.35	6.02
18	22:32:19.20	-60:32:50.1	27.42	0.60	0.35	99.99	9.99	0.35	99.99	9.99	0.35	99.99	9.99	0.35	26.59	0.49	0.35	0.79
19	22:32:19.26	-60:32:05.4	26.80	0.39	0.35	27.19	0.38	0.35	28.29	0.81	0.35	99.99	9.99	0.35	99.99	9.99	0.35	0.95
20	22:32:19.27	-60:33:20.4	99.99	9.99	0.35	99.99	9.99	0.36	99.99	9.99	0.35	99.99	9.99	0.35	99.99	9.99	0.35	1.84
21	22:32:19.31	-60:32:31.0	25.93	0.23	0.65	26.19	0.19	0.41	26.24	0.16	0.35	26.29	0.35	0.35	25.04	0.15	0.35	4.04
22	22:32:19.32	-60:32:14.7	26.36	0.31	0.35	26.08	0.17	0.36	26.17	0.15	0.41	25.41	0.16	0.35	24.90	0.13	0.36	3.02
23	22:32:19.34	-60:32:41.8	26.85	0.48	0.35	25.93	0.16	0.44	25.16	0.07	0.05	25.35	0.15	0.35	24.83	0.13	0.35	4.33
24	22:32:19.36	-60:32:35.6	23.15	0.06	0.00	22.35	0.02	0.88	21.63	0.01	0.36	20.98	0.01	0.86	20.49	0.01	0.92	24.42
25	22:32:19.39	-60:31:54.7	25.10	0.14	0.47	24.00	0.05	0.12	23.05	0.02	0.33	22.20	0.02	0.20	21.73	0.02	0.82	9.42
26	22:32:19.42	-60:31:31.2	99.99	9.99	0.35	99.99	9.99	0.35	99.99	9.99	0.35	99.99	9.99	0.35	99.99	9.99	0.35	0.64
27	22:32:19.44	-60:33:42.4	99.99	9.99	0.35	99.99	9.99	0.35	24.12	0.04	0.99	99.99	9.99	0.35	99.99	9.99	0.35	3.56
28	22:32:19.46	-60:35:41.2	27.06	0.48	0.35	25.26	0.09	0.93	26.35	0.17	0.35	99.99	9.99	0.35	25.61	0.23	0.35	2.94
29	22:32:19.47	-60:33:34.7	99.99	9.99	0.35	99.99	9.99	0.35	99.99	9.99	0.35	99.99	9.99	0.35	99.99	9.99	0.35	0.61
30	22:32:19.47	-60:34:02.5	25.72	0.19	0.35	25.35	0.10	0.07	25.44	0.08	0.48	26.59	0.45	0.35	99.99	9.99	0.35	11.98
31	22:32:19.47	-60:36:27.1	26.23	0.29	0.67	99.99	9.99	0.35	99.99	9.99	0.35	99.99	9.99	0.35	25.44	0.22	0.35	0.95
32	22:32:19.50	-60:35:06.9	26.80	0.40	0.35	26.41	0.21	0.35	26.22	0.15	0.35	26.22	0.31	0.35	25.89	0.31	0.35	2.18
33	22:32:19.52	-60:35:03.1	26.37	0.28	0.35	25.65	0.12	0.44	25.68	0.10	0.16	25.95	0.24	0.35	26.46	0.52	0.35	3.53
34	22:32:19.54	-60:34:17.6	26.14	0.24	0.35	25.91	0.14	0.36	25.89	0.12	0.35	25.71	0.20	0.35	24.79	0.12	0.35	3.71
35	22:32:19.56	-60:33:50.0	99.99	9.99	0.35	99.99	9.99	0.35	99.99	9.99	0.35	99.99	9.99	0.35	99.99	9.99	0.35	2.66
36	22:32:19.57	-60:34:58.9	26.94	0.45	0.35	26.16	0.18	0.35	25.82	0.11	0.38	26.59	0.43	0.35	27.11	0.94	0.35	4.61
37	22:32:19.57	-60:31:38.1	26.76	0.43	0.35	26.75	0.32	0.35	26.82	0.27	0.35	27.24	0.83	0.35	25.85	0.31	0.35	0.95
38	22:32:19.59	-60:34:54.7	25.04	0.12	0.01	24.72	0.06	0.04	24.85	0.06	0.01	24.87	0.09	0.35	25.17	0.16	0.35	7.83
39	22:32:19.64	-60:32:17.5	26.77	0.43	0.35	26.37	0.22	0.35	26.30	0.17	0.35	25.50	0.17	0.35	25.28	0.19	0.35	2.18
40	22:32:19.66	-60:33:01.6	24.45	0.09	0.03	24.21	0.05	0.27	24.17	0.04	0.30	23.93	0.05	0.16	23.47	0.04	0.21	9.37
41	22:32:19.67	-60:34:20.8	25.73	0.18	0.46	25.47	0.10	0.35	25.45	0.08	0.40	25.09	0.11	0.35	24.42	0.09	0.35	6.78
42	22:32:19.68	-60:32:50.6	25.23	0.14	0.49	24.83	0.07	0.10	24.94	0.06	0.11	24.88	0.10	0.11	25.34	0.20	0.35	8.24
43	22:32:19.70	-60:34:14.0	27.31	0.59	0.35	26.65	0.26	0.35	26.64	0.21	0.35	26.43	0.37	0.35	26.08	0.36	0.35	1.13
44	22:32:19.72	-60:35:51.6	25.12	0.13	0.64	26.37	0.20	0.34	26.00	0.12	0.46	26.45	0.37	0.35	25.56	0.22	0.35	3.58
45	22:32:19.73	-60:34:05.1	26.02	0.21	0.35	26.04	0.15	0.37	26.58	0.20	0.35	99.99	9.99	0.35	99.99	9.99	0.35	2.43
46	22:32:19.75	-60:33:23.7	26.75	0.37	0.35	25.71	0.12	0.05	25.17	0.07	0.61	25.39	0.15	0.35	25.09	0.15	0.35	4.74
47	22:32:19.77	-60:33:59.1	26.90	0.42	0.35	26.46	0.22	0.35	25.66	0.10	0.38	25.40	0.15	0.35	99.99	9.99	0.35	3.07
48	22:32:19.85	-60:32:04.6	27.21	0.55	0.35	25.86	0.13	0.35	26.40	0.17	0.36	27.04	0.61	0.35	26.21	0.39	0.35	2.23
49	22:32:19.85	-60:33:45.0	99.99	9.99	0.35	27.72	0.66	0.35	99.99	9.99	0.35	99.99	9.99	0.35	99.99	9.99	0.35	0.69
50	22:32:19.88	-60:34:33.7	27.31	0.58	0.35	25.79	0.13	0.18	25.24	0.07	0.34	25.14	0.12	0.35	25.10	0.15	0.35	4.17
51	22:32:19.90	-60:34:25.2	25.76	0.18	0.34	25.26	0.09	0.11	25.48	0.08	0.39	25.36	0.14	0.35	26.06	0.35	0.35	4.74
52	22:32:19.90	-60:31:40.5	25.90	0.17	0.50	25.59	0.09	0.59	25.68	0.07	0.69	25.55	0.10	0.34	25.35	0.11	0.35	0.87
53	22:32:19.95	-60:34:03.6	99.99	9.99	0.35	99.99	9.99	0.35	99.99	9.99	0.35	99.99	9.99	0.35	99.99	9.99	0.02	1.56
54	22:32:19.97	-60:33:56.3	99.99	9.99	0.35	99.99	9.99	0.35	99.99	9.99	0.35	99.99	9.99	0.35	99.99	9.99	0.35	38.30
55	22:32:19.97	-60:33:50.4	99.99	9.99	0.35	99.99	9.99	0.35	99.99	9.99	0.35	99.99	9.99	0.35	99.99	9.99	0.35	1.95

Columns (11): the total area  $A$  of the object in square arcsec;

Column (12): the half-light radius  $r_h$  in arcsec;

Column (13) and (14): minor to major-axis ratio and the position angle;

Column (15): the stellarity index computed by SExtractor in the given band. Note that faint objects have the same value of the stellarity index ( $\sim 0.35$ ) because they are beyond the classification limit ( $I \sim 22$ , see below). However, at the faint limits of the catalogs these are predominantly galaxies;

**Table 7.** HDF-South. Multi-Color Infrared Catalog from the  $\chi^2$  image in the HDF2 field.

#	$\alpha$	$\delta$	$m_J$			$m_H$			$m_K$			$A$
(1)	(2)	(3)	(4)	(5)	(6)	(7)	(8)	(9)	(10)	(11)	(12)	(13)
1	22:32:41.24	-60:35:40.6	24.69	0.31	0.46	24.70	0.69	0.35	24.29	0.32	0.44	1.00
2	22:32:41.25	-60:33:57.2	23.57	0.16	0.42	24.28	0.48	0.35	24.20	0.30	0.35	1.66
3	22:32:41.27	-60:33:59.8	23.67	0.17	0.01	24.16	0.43	0.36	23.67	0.20	0.36	2.90
4	22:32:41.27	-60:33:21.2	24.78	0.33	0.59	23.79	0.32	0.47	23.95	0.25	0.44	1.41
5	22:32:41.29	-60:33:16.6	24.87	0.35	0.36	24.54	0.60	0.34	24.05	0.27	0.46	2.57
6	22:32:41.32	-60:31:33.3	99.99	9.99	0.37	23.13	0.19	0.55	99.99	9.99	0.35	1.00
7	22:32:41.38	-60:34:14.4	24.11	0.22	0.01	24.03	0.39	0.36	23.66	0.20	0.50	3.40
8	22:32:41.43	-60:32:44.1	99.99	9.99	0.35	99.99	9.99	0.02	99.99	9.99	0.35	1.08
9	22:32:41.46	-60:32:07.8	25.57	0.55	0.36	23.88	0.34	0.36	23.91	0.24	0.19	1.24
10	22:32:41.48	-60:32:58.7	99.99	9.99	0.02	99.99	9.99	0.02	24.69	0.44	0.35	0.66
11	22:32:41.53	-60:31:21.0	22.00	0.07	0.42	21.82	0.07	0.41	22.02	0.07	0.12	14.02
12	22:32:41.53	-60:35:46.6	26.09	0.81	0.35	23.44	0.24	0.36	25.16	0.65	0.35	2.57
13	22:32:41.54	-60:35:15.7	19.80	0.03	0.03	19.64	0.03	0.04	19.46	0.02	0.04	42.22
14	22:32:41.55	-60:35:41.9	99.99	9.99	0.35	99.99	9.99	0.35	99.99	9.99	0.02	0.50
15	22:32:41.61	-60:33:29.5	24.99	0.37	0.18	24.19	0.44	0.35	24.87	0.51	0.35	1.08
16	22:32:41.61	-60:33:45.1	25.06	0.39	0.36	23.70	0.29	0.48	24.61	0.41	0.35	1.08
17	22:32:41.66	-60:34:59.5	23.71	0.18	0.00	24.13	0.42	0.35	23.62	0.19	0.01	9.04
18	22:32:41.71	-60:34:25.4	18.68	0.02	0.98	18.65	0.02	0.98	18.88	0.02	0.98	30.86
19	22:32:41.84	-60:33:60.0	23.51	0.16	0.00	23.81	0.32	0.04	22.91	0.12	0.01	10.04
20	22:32:41.89	-60:33:21.1	23.38	0.15	0.05	25.11	1.00	0.45	23.60	0.19	0.09	6.47
21	22:32:41.93	-60:34:54.8	22.74	0.11	0.02	22.33	0.10	0.67	21.98	0.07	0.24	10.78
22	22:32:41.96	-60:32:22.1	99.99	9.99	0.35	24.46	0.56	0.35	99.99	9.99	0.02	0.50
23	22:32:41.97	-60:35:21.5	25.45	0.51	0.36	23.83	0.33	0.35	23.13	0.14	0.04	8.21
24	22:32:42.08	-60:35:44.6	25.21	0.43	0.35	24.65	0.66	0.36	24.47	0.37	0.35	2.24
25	22:32:42.09	-60:31:36.2	99.99	9.99	0.35	99.99	9.99	0.03	24.62	0.41	0.47	2.65
26	22:32:42.10	-60:34:04.0	24.01	0.21	0.16	24.72	0.71	0.35	24.33	0.33	0.35	3.23
27	22:32:42.11	-60:34:08.6	23.28	0.14	0.00	22.99	0.17	0.02	23.60	0.19	0.13	5.97
28	22:32:42.14	-60:33:28.4	99.99	9.99	0.35	23.70	0.29	0.35	99.99	9.99	0.02	0.50
29	22:32:42.15	-60:33:10.3	23.26	0.14	0.00	22.95	0.16	0.02	22.78	0.11	0.64	8.88
30	22:32:42.16	-60:31:40.4	99.99	9.99	0.35	24.74	0.72	0.35	99.99	9.99	0.35	2.24
31	22:32:42.17	-60:33:34.6	23.85	0.19	0.32	23.55	0.26	0.44	23.41	0.17	0.55	4.48
32	22:32:42.19	-60:34:46.1	22.59	0.10	0.96	22.83	0.15	0.49	22.82	0.11	0.71	6.05
33	22:32:42.25	-60:32:55.1	25.53	0.54	0.42	99.99	9.99	0.35	24.62	0.42	0.44	0.75
34	22:32:42.25	-60:32:17.6	23.47	0.16	0.07	23.52	0.25	0.05	23.91	0.24	0.36	11.94
35	22:32:42.31	-60:35:31.5	22.69	0.10	0.01	22.39	0.11	0.00	22.17	0.08	0.06	15.43
36	22:32:42.31	-60:32:42.3	23.98	0.20	0.00	99.99	9.99	0.37	23.84	0.23	0.39	5.64
37	22:32:42.31	-60:33:43.0	22.12	0.08	0.18	21.74	0.07	0.16	21.54	0.05	0.97	12.69
38	22:32:42.39	-60:31:45.3	23.63	0.17	0.00	24.52	0.59	0.02	23.67	0.20	0.13	8.05
39	22:32:42.41	-60:32:35.0	24.14	0.22	0.08	24.13	0.42	0.45	24.40	0.35	0.45	3.15
40	22:32:42.42	-60:34:24.6	24.35	0.25	0.10	24.72	0.70	0.35	24.92	0.53	0.35	2.24
41	22:32:42.47	-60:31:22.4	24.59	0.29	0.15	99.99	9.99	0.35	99.99	9.99	0.35	1.99
42	22:32:42.48	-60:31:34.7	24.89	0.35	0.34	24.24	0.47	0.37	24.41	0.35	0.35	1.49
43	22:32:42.49	-60:34:31.1	24.59	0.29	0.10	99.99	9.99	0.36	23.97	0.25	0.36	2.16
44	22:32:42.54	-60:31:49.5	24.30	0.25	0.01	24.58	0.62	0.35	99.99	9.99	0.35	5.97
45	22:32:42.57	-60:35:46.8	26.11	0.83	0.35	23.76	0.31	0.35	99.99	9.99	0.35	1.00
46	22:32:42.66	-60:32:55.8	99.99	9.99	0.37	99.99	9.99	0.36	24.11	0.28	0.35	2.90
47	22:32:42.66	-60:31:28.1	25.22	0.44	0.36	24.58	0.62	0.48	99.99	9.99	0.35	1.49
48	22:32:42.67	-60:31:54.7	22.36	0.09	0.25	22.26	0.10	0.29	22.51	0.09	0.25	14.52
49	22:32:42.76	-60:31:06.5	23.60	0.17	0.00	24.32	0.50	0.35	24.45	0.36	0.42	4.89
50	22:32:42.79	-60:33:22.5	99.99	9.99	0.35	23.97	0.37	0.37	99.99	9.99	0.35	2.16
51	22:32:42.81	-60:35:47.5	99.99	9.99	0.35	24.12	0.42	0.36	99.99	9.99	0.35	0.83
52	22:32:42.84	-60:33:13.4	23.72	0.18	0.18	23.36	0.22	0.45	23.42	0.17	0.26	5.72
53	22:32:42.85	-60:33:26.0	26.21	0.89	0.35	99.99	9.99	0.02	99.99	9.99	0.35	1.08
54	22:32:42.88	-60:35:40.3	24.48	0.27	0.03	99.99	9.99	0.35	99.99	9.99	0.35	2.65
55	22:32:42.88	-60:32:10.7	20.78	0.04	0.03	20.52	0.05	0.01	20.44	0.04	0.03	26.54

Column (16): SExtractor flags.

A total of five single optical-passband catalogs (*UBVRI*) are available for HDF2 comprising 1227 objects in *U*, 2018 in *B*, 2071 in *V*, 1233 in *R* and 1297 in *I*. Object catalogs have also been extracted from the infrared images and Table 5 illustrates

the information available for single-band infrared catalogs. It shows the first page of the deep *Ks*-band catalog extracted from the HDF2 images which overlap the HST-WFPC2 region. The infrared catalogs comprise 905 objects in *J*, 525 in *H* and 638 in *Ks*. For HDF1 the infrared catalogs have been constructed



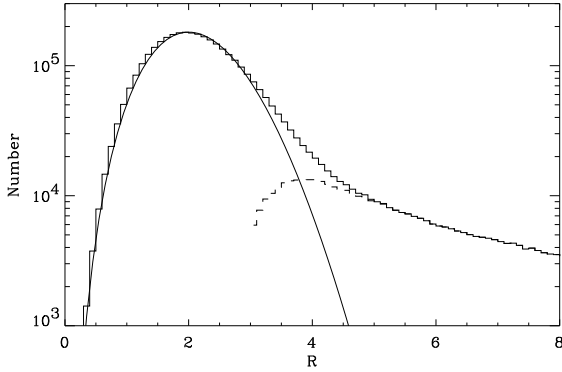


**Fig. 6.** The  $R$  distribution (solid histogram) for the  $\chi^2$ -image produced by co-adding the optical data ( $N = 5$ ). This distribution is compared to the expected  $R$  distribution for pure Gaussian noise (solid line), showing the excess tail at high  $R$ -values, due to pixels containing object flux (dashed line).

and comprise of 415 objects in  $J$ , 439 in  $H$  and 594 in  $K_s$ . Note that the limiting magnitudes vary for different pointings and bands (see Table 3). The ASCII version of these catalogs are available at “<http://www.eso.org/eis>”.

### 3.2. Multi-band Catalogs

Using the single passband catalogs presented in the previous section a multi-color catalog can be built by the association of sources identified in the different passbands. An alternative is to carry out the detection in some suitably chosen reference image and measure the photometric quantities in each passband using the same circular or isophotal aperture as measured in the reference image, thereby assuring a one-to-one correspondence. In the past, different choices have been made regarding the choice of this reference image (e.g., Williams *et al.* 1997, Arnouts *et al.* 1998, Szalay, Connoly & Szokoly 1998). Without discussing the merits of each of these options, and after some experimentation using either  $R + I$  or  $I$  as the reference the  $\chi^2$  method advocated by Szalay, Connoly & Szokoly (1998) has been adopted.

The method takes into account all the multicolor information available. Since all photometric bands are registered to a common reference system, each pixel has measured fluxes  $f_i$ ,  $i = 1 \dots N$ , with  $N$  the number of photometric bands. ( $N = 3$  for SOFI data,  $N = 5$  for SUSI2 data, and  $N = 8$  for the combined optical and infrared data). For each band the local mean background  $\mu_i$  and its standard deviation  $\sigma_i$ , have also been determined. Therefore, each pixel can be described by an  $N$ -dimensional vector, whose length  $R$  is given by

$$R^2 = \sum_{i=1}^N \frac{(f_i - \mu_i)^2}{\sigma_i^2}. \quad (1)$$

The probability distribution for  $R^2$  is then a  $\chi^2$  with  $N$ , degrees of freedom, or, for  $R$

$$dP(R) = \frac{1}{2} R^{N-1} e^{-R^2/2} dR. \quad (2)$$

Hence, by subtracting the backgrounds  $\mu_i$ , dividing by  $\sigma_i^2$ , and subsequent co-addition of the squared images, a new image of  $R^2$  values is created. This  $\chi^2$ -image, measures the cumulative probability  $P(> R)$  that a pixel is drawn from the sky distribution. In practice the square-root (e.g.  $R$ ) image is analyzed.

Figure 6 shows the  $R$  distribution for the  $\chi^2$ -image that was produced by co-adding the optical data ( $N = 5$ ). This distribution is compared to the expected  $R$  distribution, showing an excess tail at high  $R$ -values, due to pixels containing object flux. The difference between the measured distribution and the expected noise distribution gives the distribution of  $R$ -values for pixels containing object flux, and the ratio of the noise distribution and object distribution provides a good measure of the probability that a given  $R$  value is due to the presence of an object. In principle, one could use the  $R$ -value for which the number of object pixels exceeds the number of noise pixels, as a threshold value for SExtractor, taking the  $\chi^2$ -image as the detection image, and the single-band images as the analysis image. However, in practice, one would like to take into account the correlation of object flux over several pixels, to further enhance the sensitivity to faint objects.

The procedure adopted for the present work was to convolve the background subtracted co-added single band images with a Gaussian with 1 arcsec FWHM and compute its rms noise ( $\sigma_i$ ). These convolved images were then normalized by their respective rms maps, squared and added to produce the  $\chi^2$  image. In order to determine the threshold and the minimum number of pixels to be used as a detection criterion in SExtractor, empty images, containing randomly generated noise, were created. In these random images the number of ‘false’ objects as a function of detection parameters was determined, thus providing both a detection threshold and the minimum number of contiguous pixels, which minimize the number of false detections. These detection parameters were used to construct a first set of catalogs for the science images. The detection threshold was then lowered in several steps, until the number of additional sources in the subsequent catalog became smaller than twice the number of false sources that would be included by similarly lowering the threshold in the random image. Hence, by design, at the lowest signal to noise levels, the catalogs are roughly 50% reliable.

This method was used to compile a multi-color optical catalog for HDF2, comprising 2862 objects. This catalog gives for each object detected on the  $\chi^2$  image, built from the combination of the  $UBVRI$  co-added images, the following parameters. The first three columns give the entry number in the table (not to be misinterpreted as a unique reference to a specific object), the right ascension and declination (J2000.0) as determined in the detection image. These columns are followed by three columns for each passband considered (depending on the specific sample), listing the magnitude, the error and the stel-

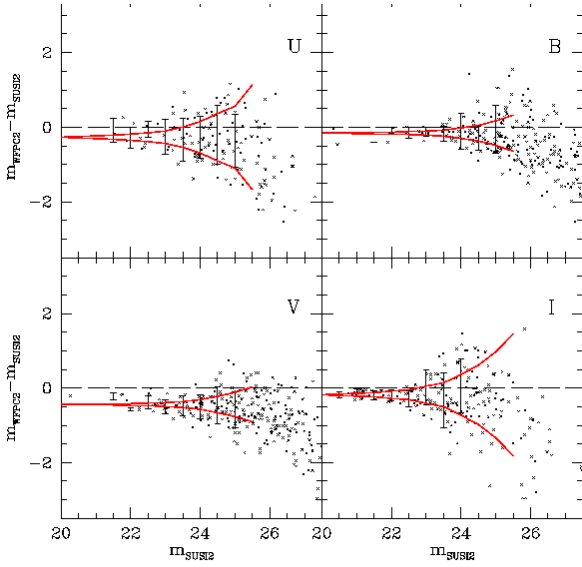


**Fig. 7.** Comparison between total magnitudes computed from the WFPC2 image, convolved with a Gaussian of FWHM of 1 arcsec, with those measured in the SUSI2 fields for the different passbands indicated in each panel.

larity index. The final column gives the area of the object as measured in the detection image in square arcsec. For large objects, with a detection area larger than the aperture of 2 arcsec in diameter, the magnitude is measured within the isophotal area. For smaller objects, the magnitude is measured in the 2 arcsec aperture. For objects with  $S/N \leq 1$ , the magnitude is set to 99.9 and the error to 9.99 to indicate a detected object with insufficient flux in the given band. In the Table 6 only the first 55 entries of this catalog are shown.

A discussion on the performance of this procedure for detecting objects is discussed in Section 5. Two similar catalogs are also available listing infrared colors for the two SOFI fields comprising 1424 objects in HDF1 and 1530 in HDF2, respectively. Table 7 lists the first 55 entries of the infrared catalog produced for the HDF2 field. The format is similar to that presented in the previous table. Finally, Table 8 lists the first 55 objects extracted from the combined optical-infrared  $\chi^2$  image. The corresponding catalog contains 1202 objects detected within the HDF2 SOFI-SUSI2 overlap, which covers the HST-WFPC2 field. Of the 1202 objects detected in the combined  $UBVRIJHKs$  catalog, 479 objects have measurable magnitudes in all the individual passbands; 52 objects in none of the individual passbands; and 61 in only one of the passbands. Most of the latter 61 objects have a measurable magnitude in either the blue ( $U$  or  $B$ ) or red ( $J$  or  $Ks$ ) passbands.

#### 4. External Comparison

To check the photometric accuracy of the EIS-DEEP data, these were compared to other ground-based observations of the field, which include data from the Anglo-Australian Observa-

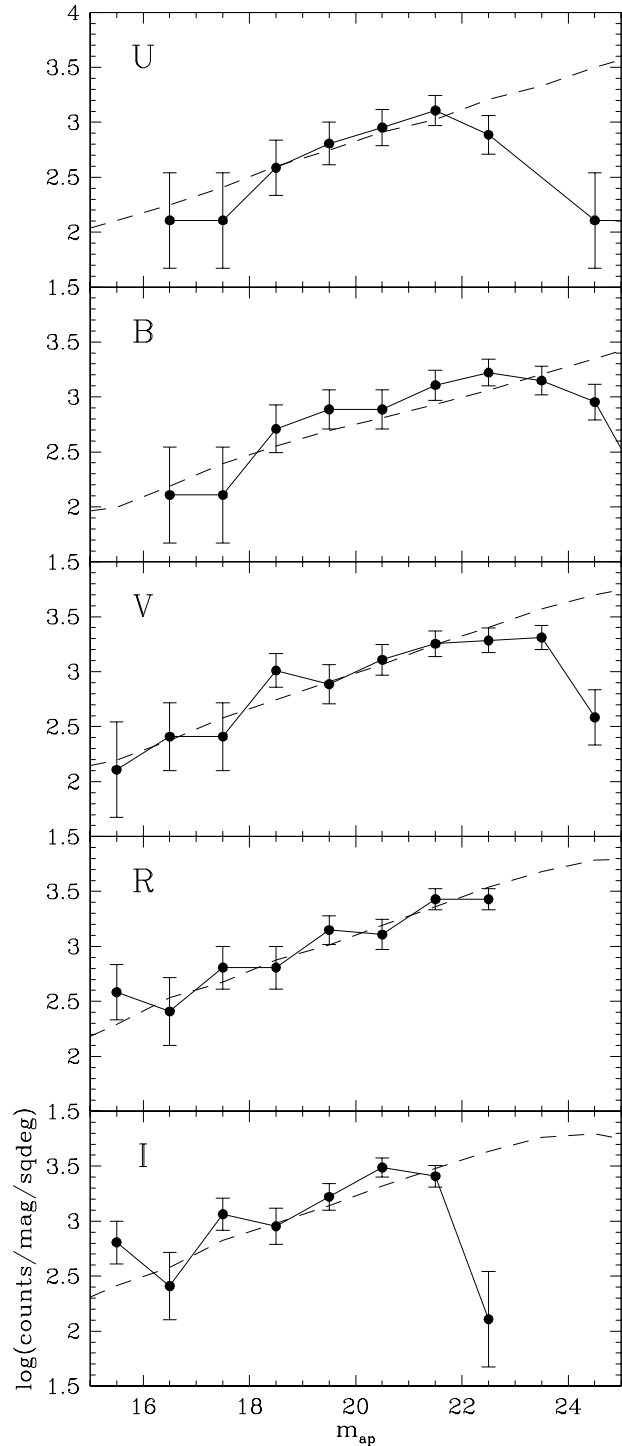


**Fig. 8.** Comparison of the observed star-counts (filled circles) with model predictions as described in the text (dashed line).

tory (AAO, available from the web) and data obtained using the VLT-UT1 Test Camera during the Science Verification period (see ESO home page). These comparisons were done by comparing object catalogs extracted using SExtractor and the zero-points as provided by the original references. A direct com-

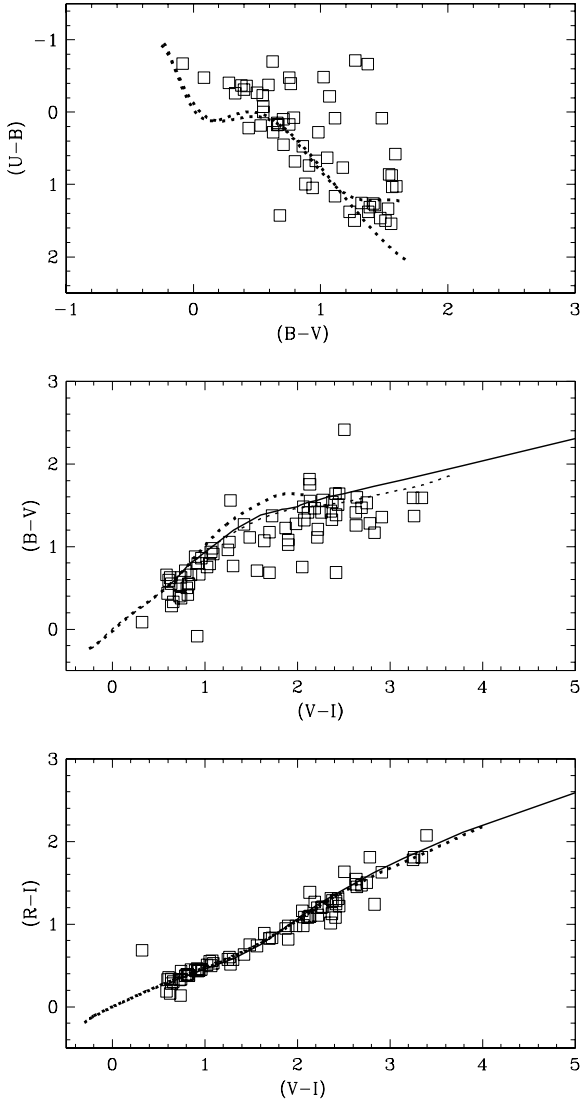


**Fig. 9.** Color-color diagrams for point sources in the HDF2 field compared with empirical determinations (dashed line) and model predictions (solid line). Only  $5\sigma$  detections are included and the number of points shown are 58, 75 and 77 from the top to the bottom panel.

parison with the AAO data yields in  $R$ -band a mean difference  $\langle R_{NTT} - R_{AAO} \rangle = 0.02$  mag and an rms of 0.08 mag in the range 17.0-22.5. In the  $B$ -band, the mean difference is found to be 0.12 mag and the rms  $\sim 0.17$  mag, in the magnitude range 16.0-24.0. Comparing the present data with those in  $R$  band obtained from the VLT-UT1 test camera images, one finds an rms  $\sim 0.13$  mag down to  $R=25$ . Unfortunately, there is no independent zero-point for the  $R$  image obtained with the test camera.

Using the HST-WFPC2 HDF-S observations catalogs were extracted for each passband at full-resolution, as well as at a resolution comparable to that of the SUSI2 images (by convolving the WFPC2 image with a Gaussian with a FWHM of 1

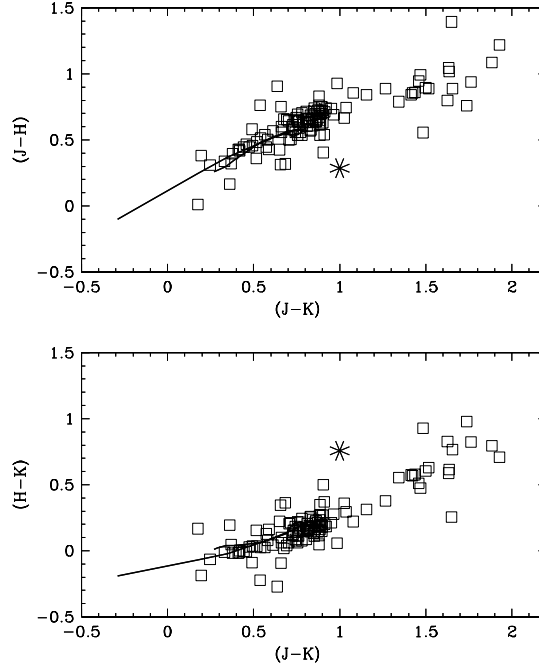


**Fig. 10.** Infrared color-color diagrams for point sources in the HDF2 field compared with model predictions (solid line). Also shown is the QSO in the STIS field (star).

arcsec). These data have been used to further check the photometric and astrometric calibration of the NTT data and to evaluate the reliability of the detections. Figure 7 shows the comparison of the magnitudes derived from SExtractor for sources detected on the convolved WFPC2 image with those measured from the co-added SUSI2 for each available passband. Also shown are the errors computed by SExtractor and the scatter, computed in 0.5 mag bins directly from the comparison of the two data sets. The results show that while there are differences in zero-points, expected because of the different passbands of the filters, the scatter is consistent with the errors estimated by SExtractor.

To test the accuracy of the derived astrometric solution the position of the objects detected in the  $\chi^2$  image, created by combining the multi-band SUSI2 images, were compared with the HST-WFPC2 images and the relative shift in positions measured. Relative to the WFPC2 detections, the EIS objects are displaced to the northeast. The amplitude of the shift is 0.11 arcsec in right ascension and 0.4 arcsec in declination relative to that used by STScI. Furthermore, based on this comparison the internal accuracy of the astrometric solution is estimated to be  $\lesssim 0.4$  arcsec. The measured shift is consistent with the error of the USNO-A V1.0 catalog used in the present paper relative to the more accurate astrometric reference catalog used in the analysis of the HDF-S data.

The results presented in this section demonstrate that the photometric zero-points, errors in the magnitude measurements



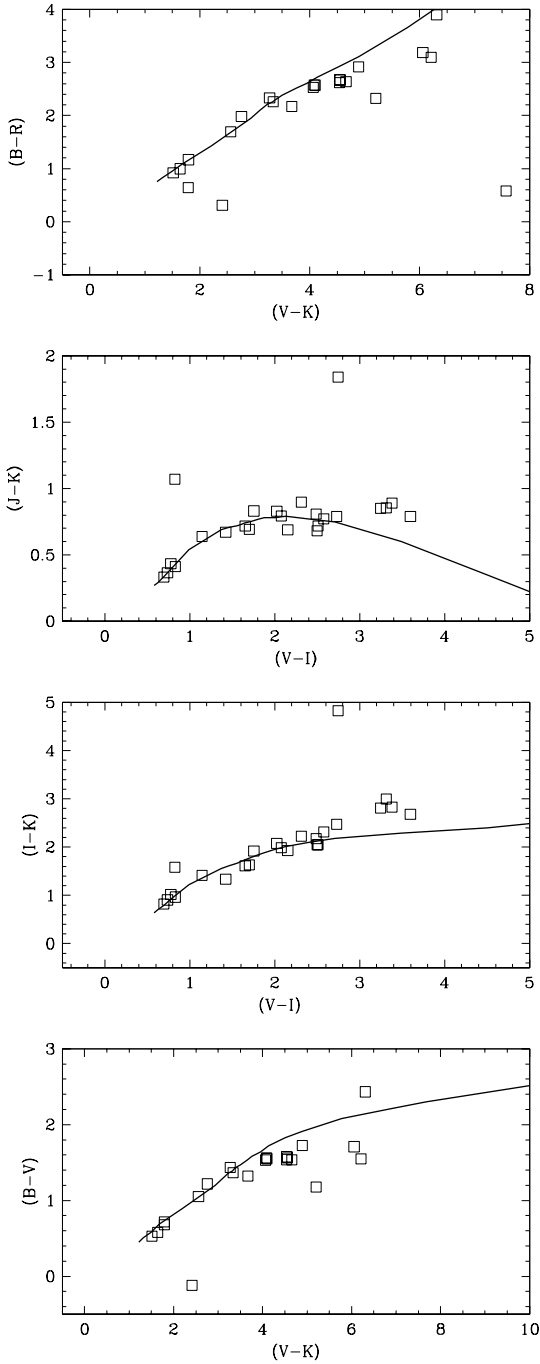


**Fig. 11.** Optical-infrared color-color diagrams for point sources in the HDF2 field compared with model predictions (solid line).

and the astrometric solution obtained in the present paper are reliable.

## 5. Discussion

For a preliminary evaluation of the overall quality of the photometric calibration and object detection, photometry and classification, in this section simple statistics such as galaxy and

star number counts, and color-color diagrams produced from the catalogs described above are compared with other available data. Since optical data are only available for HDF2, the following discussion will concentrate on this region, unless otherwise specified.

### 5.1. Point-Sources

To facilitate comparisons with other data sets, throughout this section magnitudes are expressed in the Johnson-Cousins system. Even though the number of stars in the HDF2 field is relatively small ( $\sim 80$ ), it is of interest to compare the star counts with model predictions, thus providing an indication of the classification limit. Figure 8 compares the measured star counts in the HDF2 field, for each optical passband available, with the galactic model predictions of the Besancon Observatory group (*e.g.*, Haywood, Robin, & Creze 1997). Stars are defined to be sources with a stellarity index  $\geq 0.85$  in the *I*-band. The observed counts are in good agreement with the model predictions down to the classification limit which corresponds  $U \lesssim 22.5$ ,  $B \lesssim 24.0$ ,  $V \lesssim 24.0$ ,  $R \lesssim 22.5$ , and  $I \lesssim 22.0$ .

The stellar color-color diagrams also offers an important diagnostic to evaluate the data. From the comparison of the observed stellar track with other data and/or with model predictions for different color combinations one is able to detect any systematic errors in the photometric calibration. Exploration of the multi-dimensional color space from data in eight passbands may also reveal interesting population of objects.

From the many possible optical colors combination, Figure 9 shows three examples involving all the passbands used. All the colors have been corrected for reddening and the  $(U - B)$  and  $(B - V)$  colors have been corrected for the color term derived in section 2.2. To minimize contamination by spurious objects and/or unresolved galaxies, only  $5\sigma$  detections, in all passbands, are included in these diagrams. For comparison, the empirical relations compiled by Caldwell *et al.* (1993) and, whenever available, a theoretical isochrone taken from Baraffe *et al.* (1997) are used because they provide color information in the infrared. The theoretical model assumes a 10 Gyr,  $[M/H] = -1$  population, more typical for halo stars, and is fine-tuned to model low-mass main sequence stars. As it can be seen, in all cases the EIS-DEEP data are in good agreement with the empirical and/or model sequences, with all the known features of the stellar population of the main components of the galaxy easily recognizable. For instance, objects with  $(B - V) \sim 0.5$  and  $(U - B) \sim -0.2$  are low metallicity halo stars near the turnoff, located at few kpc from the Galactic plane, while the red population with  $(B - V) \sim 1.3$  and  $(U - B) \sim 1.3$  consist of faint disk M-dwarfs. These two populations are easily seen in the  $(U - B) \times (B - V)$  diagram.

Potentially interesting objects can be isolated in the multicolor space from their departure from the stellar sequence. One such an example is the blue object at  $(B - V) \simeq -0.1$  and  $(V - I) \simeq 0.9$  ( $V \sim 20.1$ ), lying in a region typical of low-redshift ( $z < 1.0$ ) quasars (*e.g.*, Zaggia *et al.* 1998). This object also shows distinct optical-infrared colors (see Figure 11).

Infrared colors for 130 star-like objects with  $K \leq 20$  from HDF1 and HDF2 fields are shown in Figure 10. Again, the data are compared to the Baraffe *et al.* (1997) model. Also shown are the infrared colors of the QSO ( $(J - K) = 1.0$ ,  $(H - K) = 0.73$ ) at  $z \sim 2.2$  centered in the STIS camera. Note that the data extends well beyond the theoretical track which, according to the model, should have a concentration at  $(J - K) \simeq 0.8$  and  $(J - H) \simeq 0.6$ . The sparse population at  $(J - K) > 1.2$  and  $(J - H) \simeq 1.0$  are probably unresolved background galaxies contaminating the stellar sample. In fact, by setting the limit on the stellarity index to 0.95, most of these objects disappear from the diagram. Finally, combinations of optical and infrared colors for 25 star-like objects in the region of overlap between SUSI2-SOFI are presented in Figure 11, showing again good agreement with the theoretical model. In summary, the good agreement between the data and empirical/model stellar in the optical, infrared and optical-infrared color diagrams are evidences of the accuracy of the optical and infrared zero-points in the different passbands used.

## 5.2. Galaxies

To evaluate the performance and depth of the galaxy catalogs produced in the different optical passbands, the number counts obtained within the region defined by the master mask (Section 2.1), with an area of about  $5.3 \times 5.3$  square arcmin, are shown in Figure ???. In the catalogs galaxies are defined to be objects with a stellarity-index less than 0.85 and SExtractor flags  $< 4$ . The counts obtained by other authors from deep imaging of smaller regions (*e.g.*, Smail *et al.* 1995, Williams *et al.* 1996, Arnouts *et al.* 1998) are given for comparison. The error-bars in the histograms are simply the Poisson errors. As can be seen, there is a remarkable agreement between the EIS-DEEP galaxy-counts and those of the other authors over a broad range of magnitudes. The most significant difference is the observed flattening of the  $I$ -band counts in the range  $I_{AB}=25$ -26. This is probably due to the fringing correction which, as pointed out earlier, may affect the detections at faint flux levels. As emphasized earlier the depth in  $U$ -band is remarkably close to the limit achieved with the HST-WFPC2 camera. Using the HDF counts as a reference the completeness limit of the catalogs is roughly  $U_{AB} = 27$ ,  $B_{AB} = 26.7$ ,  $V_{AB} = 26$ ,  $R_{AB} = 25.5$  and  $I_{AB} = 25$ . The density of galaxies ranges from 28 to 70 galaxies per square arcmin.

In order to evaluate the performance of the  $\chi^2$  detection method used in the production of multi-band catalogs, in Figure ??? the distributions of galaxy number counts obtained from the  $\chi^2$  detections are compared with those obtained in each passband. As can be seen there is a dramatic increase in the number of detections, especially in the  $U$ ,  $R$  and  $I$ -bands. which in some cases is as large as a factor of 3. Of course, these detections are primarily at the faint end. The reliability of the detections obtained from the  $\chi^2$  image is impressive. Visual inspection of the detections, using the HST-WFPC2 observations, indicates that the overall reliability of the  $\chi^2$  detections is 93%. For objects with  $I < 26$ , the reliability is better than

95%, implying a gain of about 1 mag in the limiting magnitude. The reliability decreases to 45% for detections corresponding to objects for which the measured isophotal  $I$ -band magnitude in the co-added image is fainter than  $I=28$ .

Similarly, in Figure ?? the counts in the infrared passbands are shown combining the two fields observed, based both on detections in single bands and in the  $\chi^2$  image built from the combination of the  $JHKs$  images. As in the case of the optical catalogs, the multi-color catalogs extracted from the  $\chi^2$  image extend to much fainter magnitudes and have an excellent reliability.

Since one of the primary goals of the survey has been to identify candidate galaxies at high- $z$  for follow-up spectroscopic observations with the VLT, the color information available in optical, infrared and optical-infrared has been used to identify preliminary candidates. Extensive work has been done to tune the color-selection criteria for the HST filters (*e.g.*, Madau *et al.* 1996) and to identify regions in the color-color diagrams populated by Lyman-break galaxies in different redshift ranges. However, the differences in the passbands between the SUSI2 and WFPC2 filters prevent using the same color criteria. It is important to emphasize that, in general, any U-dropouts in the filters used by SUSI2 would lead to the identification of galaxies at larger redshifts because of the shift to red of the SUSI2 passband, and consequently to a smaller density of objects than that inferred by Madau *et al.* (1996). However, given the great interest in finding likely candidates at high- $z$  a simple approach has been adopted here for a first cut analysis. This was done by considering the tracks most likely to trace the evolutionary sequence of galaxies of different types in color-color diagrams appropriate for the SUSI2 filters (Arnouts 1998, see also Fontana *et al.* 1998). Based on these results conservative regions in  $(U - B) \times (B - I)$  and  $(B - V) \times (V - I)$  diagrams, shown in Figure 16, were defined. The criteria adopted were  $(U - B)_{AB} \gtrsim 1.5$  and  $(B - I)_{AB} \lesssim 2$  in the  $(U - B) \times (B - I)$  diagram and  $(B - V)_{AB} > 1.5$  and  $(B - V)_{AB} > 2 \times (B - I)_{AB} - 0.14$ . Based on the model predictions these regions should be populated by  $z > 3$  galaxies. A more precise selection will require a more detailed analysis using the color information to assign photometric redshifts. This will certainly be pursued by several groups using the public data.

The galaxies shown in Figure 16 are detections obtained from the optical  $\chi^2$  image, thus allowing for the identification of objects that may be undetected in one or more passbands. The objects shown in the color-color diagrams follow several constraints. First, they have to be  $\geq 2\sigma$  detections at least in  $B$  and  $I$  for the diagram shown in the left panel and  $V$  and  $I$  for that in the right panel. If the object is less than a  $2\sigma$  detection in the bluest passband, it is represented as a triangle, otherwise as a circle. For blue dropouts the magnitude measured by SExtractor was used regardless of its error. If the magnitude is not measurable ( $m=99.9$ ), the  $2\sigma$  limiting magnitude is assigned to the object.

Adopting this procedure galaxies the HDF2 field covering  $\sim 28.1$  square arcmin were selected. A total of about 120 can-

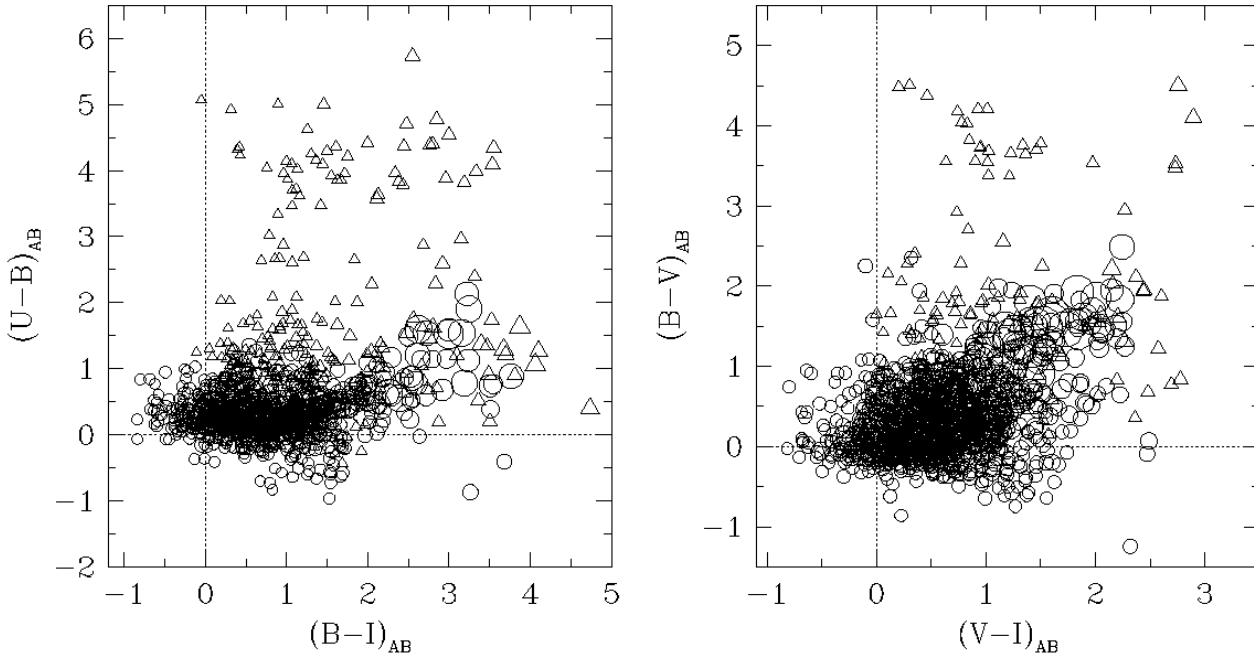


**Fig. 16.** Galaxy  $(U - B) \times (B - I)$  and  $(B - V) \times (V - I)$  color-color diagrams. In the plot the selection boxes proposed by Madau *et al.* (1996) to identify galaxies in the redshift ranges  $3 < z < 4$  (left panel) and  $z > 4$  (right panel) are also shown. The size of the symbols are inversely proportional to the  $I$ -band magnitude of the galaxy.

didates satisfied at least one of the criteria mentioned above. Given the large uncertainties in the adopted procedure no attempt has been made to assign these objects to any redshift range. All candidates were visually inspected and about half of them were discarded for the following reasons: 1) close to edge of the frame; 2) near relatively bright stars; 3) close to masked out regions; and 4) lying along spikes from the bright stars in and near the field. The remaining objects, likely to be promising candidates, are listed in Table 9. The table provides the following information: in columns (1) and (2) right ascension and declination (J2000.0); in column (3) the  $I_{AB}$  magnitude. The remaining columns give the colors and their respective errors. Note that there are 20 galaxies within the region of overlap between SUSI2 and SOFI (12.8 square arcmin), and for them the optical-infrared ( $I - K$ ) color is also provided. Whenever, an object is undetected in a given passband or the  $S/N < 1$  the error in the color involving this filter is set to -1. In Figure 17 some examples of likely high-redshift galaxies are shown to illustrate the type of candidates that have been selected. Finally, note that inspection of the  $(V - I) \times (I - K)$  diagram allowed to isolate one possible V-dropout candidate (number 36 in the table), shown in the last row of Figure 17. Even though the selection criteria adopted are admittedly crude, inspection of the selected objects indicates that they are by and large promising.

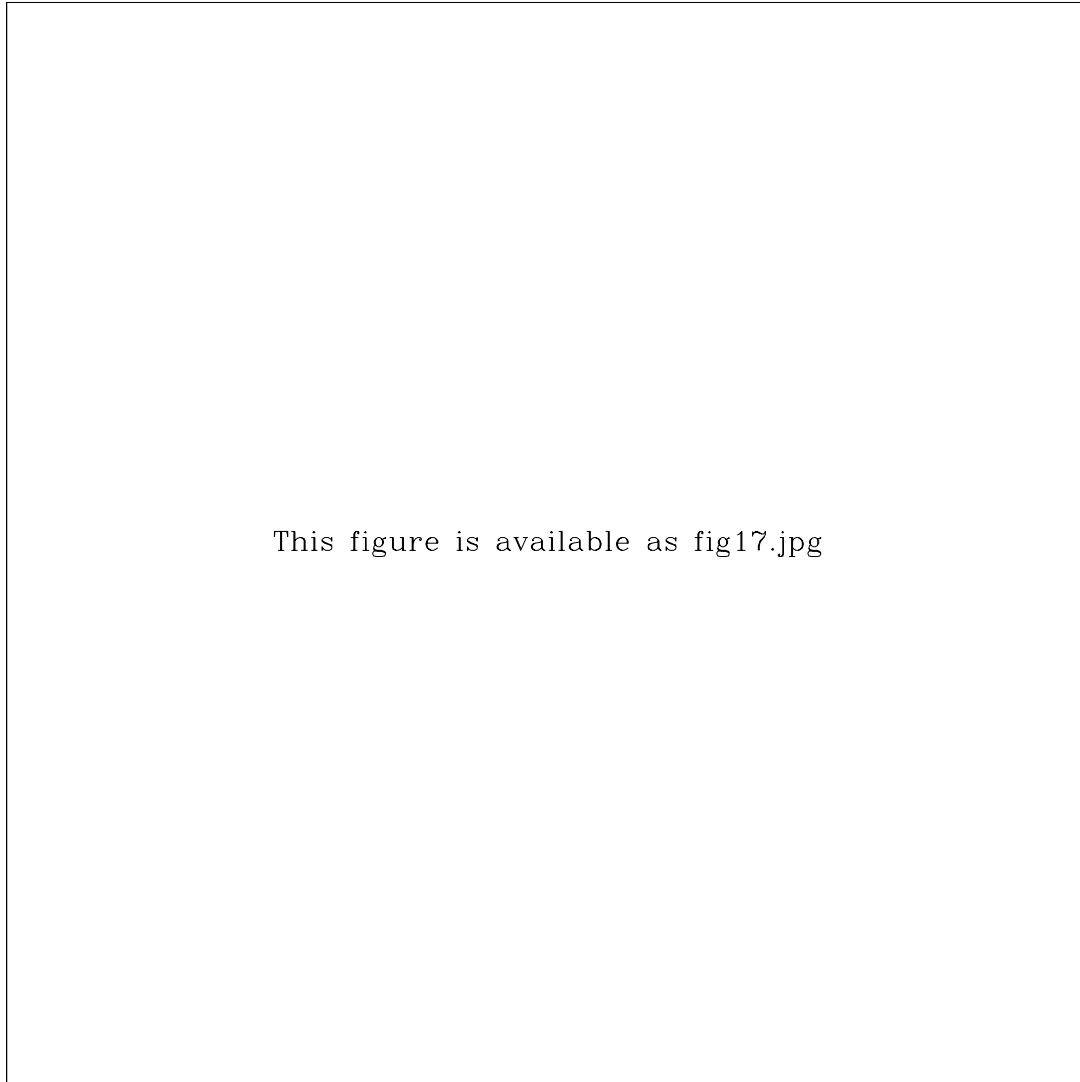
## 6. Summary

This paper presents the results of deep optical ( $\sim 30$  square arcmin) and infrared ( $\sim 40$  square arcmin) imaging of two

regions which include the HST-WFPC2 and STIS fields. The former has been covered in eight passbands from the optical to the infrared, while the latter in two optical and three infrared passbands. The observations were carried out as part of the EIS public survey. In addition single-passband catalogs have been prepared as well as multi-color optical, infrared and optical-infrared catalogs. The latter were produced using the  $\chi^2$  technique. Preliminary results have shown that the method is rather promising leading to robust detections of very faint galaxies. The color information has been used to find possible high- $z$  galaxies for follow-up observations with the VLT. All the data presented here, in the form of images and catalogs, are being made public world-wide and can be requested at "<http://www.eso.org/eis>". It is expected that these EIS-DEEP data, covering a larger area and with deep infrared coverage, will further contribute to future studies of the HDF-S region.

*Acknowledgements.* We thank all the people directly or indirectly involved in the ESO Imaging Survey effort. In particular, all the members of the EIS Working Group (S. Charlot, G. Chincarini, S. Cristiani, J. Krautter, K. Kuijken, K. Meisenheimer, D. Mera, Y. Mellier, M. Ramella, H. Rotterling and P. Schneider) for the innumerable suggestions and criticisms, the ESO OPC, the NTT team, in particular the night assistants, the ESO Archive Groups and ECF. We would also like to thank S. Arnouts, J. Caldwell, N. Devillard, A. Fontana and R. Fosbury for their help and assistance. Special thanks to Riccardo Giacconi for making this effort possible.

## References



This figure is available as fig17.jpg

**Fig. 17.** Examples of objects selected as likely high-redshift galaxies. Each row shows postage stamps extracted from the images in different passbands showing *UBVIR* from left to right. The selected objecta are at the center of each postage stamp.

- Arnouts S., D'Odorico S., Cristiani S., Zaggia S., Fontana A., & Giallongo E., 1999, A&A, in press
- Baraffe I., Chabrier G., Allard F., & Hauschildt P. H., 1998, A&A, in press
- Bertin, A. & Arnouts, S., 1996, A&AS, 117, 393
- Caldwell, J., Cousins A., Ahlers C., van Wamelen, & Maritz E., 1993, SAAO Circulars, 15, 1
- Devillard, N., 1998, Eclipse Data Analysis Software Package (ESO: Garching)
- D'Odorico, S. *et al.*, 1998, Proceedings of SPIE 3355, p. 507
- Fruchter, A.S. & Hook, R. N., 1998, PASP, submitted (astro-ph/9808087)
- Haywood, M., Robin, A.C., & Creze, M., 1997, A&A, 320, 440
- Landolt, A.U., 1992, AJ, 104, 340
- Madau, P., Ferguson, H. C., Dickinson, M. E., Giavalisco, M., Steidel, C. C., & Fruchter, A. 1996, MNRAS, 283, 1388
- Moorwood, A., Cuby, J.G. & Lidman, C., 1998, The Messenger, 91, 9
- Nonino *et al.*, 1998, AA, in press, (astro-ph/9803336)
- Persson, 1997, private communication
- Schlegel, D. J., Finkbeiner, D. P., & Davis, M. 1998, ApJ, 500, 525
- Smail, I., Hogg, D.W., Yan, L., Cohen, J.G., 1995, ApJ 449, L105
- Szalay, A., Connolly, A. & Szokoly, G. P. 1998, astro-ph/9811086
- Zaggia *et al.*, 1998, AA, in press, (astro-ph/9807152)

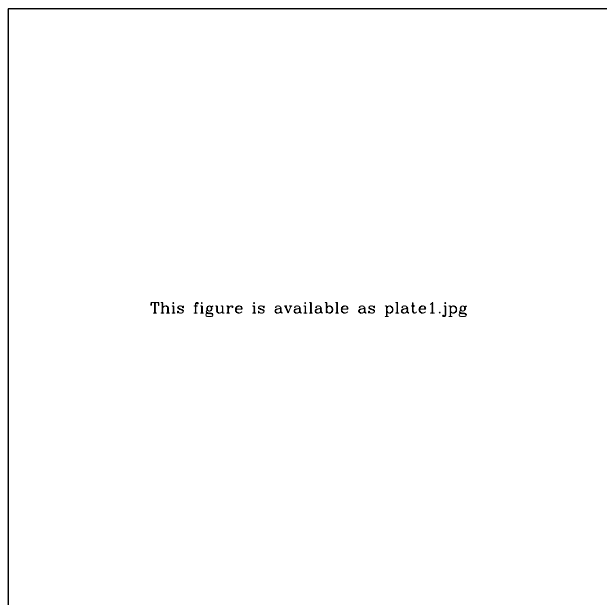


**Fig. 18.** True-color image of the HDF2 field based on the five observed optical passbands. The blue channel is represented by the *UB*-band images, the green channel by the *VR*-band images, and the red channel by the *I*-band image. The edges of the field have been trimmed to include only pixels with a sensitivity  $\gtrsim 70\%$  in all passbands.

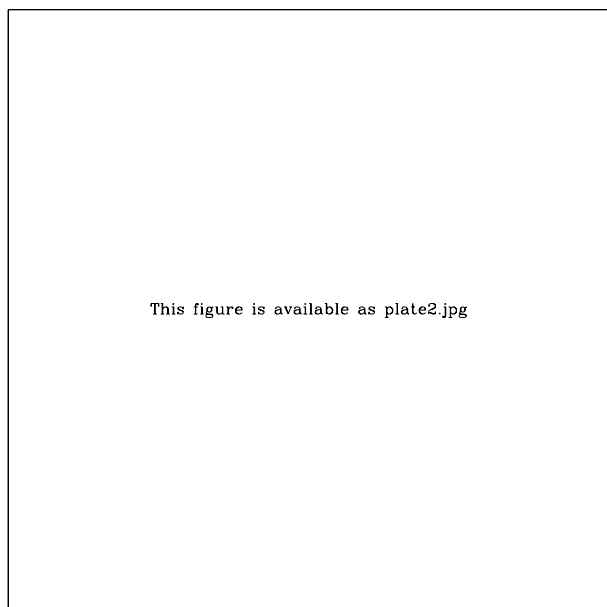


**Fig. 19.** True-color image of part of the HDF2 field for which the optical and infrared observations overlap. The region includes most of the HST-WFPC2 field. The image is, perhaps, one of the most colorful pictures available, being based on 8 passbands covering an extended spectral region from 300 to 2200 nm. The blue channel is represented by the combination of the *UBV*-band images, the green channel by the *RI*-band, and the red channel by the *JHKs*-band images. This color image covers an area of approximately  $2.5 \times 4.0$  square arcmin corresponding to the SUSI2-SOFI overlap covering the HST-WFPC2 field.

**Table 9.** High-z Galaxy Candidates

#	$\alpha$	$\delta$	$m_{ap}$	$(U-B)$	$\epsilon$	$(B-V)$	$\epsilon$	$(V-I)$	$\epsilon$	$(B-I)$	$\epsilon$	$(R-I)$	$\epsilon$	$(I-K)$	$\epsilon$
1	22:32:20.42	-60:31:49.9	25.54	0.59	-1	1.65	0.57	0.00	0.32	1.65	0.63	0.01	0.36	-	-
2	22:32:20.83	-60:35:52.5	25.44	3.02	-1	0.42	0.25	0.36	0.28	0.79	0.33	0.14	0.31	-	-
3	22:32:21.10	-60:34:51.0	25.40	1.55	-1	0.54	0.33	0.66	0.29	1.20	0.37	0.13	0.30	-	-
4	22:32:22.13	-60:35:09.0	25.83	3.96	-1	0.75	0.34	0.21	0.35	0.96	0.44	-0.12	0.38	-	-
5	22:32:22.40	-60:35:09.3	25.22	1.73	0.93	0.50	0.17	0.05	0.22	0.55	0.25	-0.23	0.24	-	-
6	22:32:22.63	-60:35:29.3	25.95	-0.37	-1	3.74	-1	0.95	0.50	4.69	-1	0.24	0.51	-	-
7	22:32:22.64	-60:33:03.0	26.17	-2.21	-1	3.56	-1	0.90	0.61	4.47	-1	-0.13	0.57	-	-
8	22:32:22.75	-60:32:59.1	24.91	1.68	1.02	0.47	0.19	0.49	0.19	0.95	0.23	0.19	0.21	-	-
9	22:32:22.93	-60:34:29.9	25.38	2.85	-1	1.56	0.61	0.51	0.28	2.07	0.64	-0.00	0.29	-	-
10	22:32:26.00	-60:34:51.2	25.82	4.15	-1	0.89	0.37	0.11	0.38	1.00	0.49	-0.52	0.38	-	-
11	22:32:26.56	-60:35:32.1	25.77	5.01	-1	0.42	0.35	0.47	0.38	0.89	0.45	0.32	0.45	-	-
12	22:32:27.59	-60:32:58.5	25.61	1.89	-1	2.41	1.41	0.35	0.34	2.76	-1	-0.40	0.34	-	-
13	22:32:27.64	-60:33:51.8	26.15	4.04	-1	0.53	0.42	0.22	0.51	0.76	0.60	0.47	0.68	-	-
14	22:32:27.90	-60:34:11.6	25.28	0.58	1.26	1.50	0.49	0.41	0.25	1.92	0.52	0.04	0.27	-	-
15	22:32:29.74	-60:35:58.1	25.11	3.86	-1	1.06	0.35	0.61	0.22	1.67	0.38	0.58	0.28	-	-
16	22:32:29.83	-60:35:33.3	26.00	-0.41	-1	3.82	-1	0.85	0.51	4.67	-1	0.22	0.54	-	-
17	22:32:30.68	-60:36:16.2	24.34	2.82	-1	2.02	0.58	1.02	0.14	3.04	0.58	0.29	0.13	-	-
18	22:32:30.95	-60:32:43.8	24.77	0.39	1.20	1.84	0.52	0.61	0.18	2.45	0.53	0.33	0.20	-	-
19	22:32:30.99	-60:36:16.7	25.28	2.56	-1	1.68	0.74	0.72	0.26	2.40	0.76	0.13	0.27	-	-
20	22:32:31.00	-60:35:32.1	25.52	-0.38	-1	4.21	-1	0.93	0.35	5.14	-1	0.33	0.37	-	-
21	22:32:31.07	-60:33:29.7	25.49	2.68	-1	0.89	0.27	0.02	0.29	0.91	0.36	-0.35	0.30	-	-
22	22:32:31.28	-60:33:25.3	24.94	4.36	-1	1.34	0.29	0.26	0.19	1.61	0.33	0.07	0.21	-	-
23	22:32:31.87	-60:35:15.9	24.23	-0.39	1.34	2.56	0.94	1.16	0.14	3.71	0.94	0.61	0.14	-	-
24	22:32:32.56	-60:34:14.8	24.96	4.22	-1	0.76	0.35	0.99	0.23	1.75	0.36	0.13	0.21	-	-
25	22:32:33.30	-60:31:37.2	25.24	0.24	-1	4.48	-1	0.21	0.24	4.68	-1	0.34	0.30	-	-
26	22:32:34.08	-60:36:13.3	25.35	4.10	-1	0.63	0.38	0.81	0.29	1.44	0.41	-0.15	0.27	-	-
27	22:32:34.98	-60:33:36.5	25.17	2.65	-1	0.89	0.45	0.94	0.27	1.83	0.46	0.26	0.27	-	-
28	22:32:35.92	-60:34:54.4	25.42	4.25	-1	0.87	0.35	0.44	0.29	1.30	0.40	0.62	0.39	-	-
29	22:32:35.96	-60:32:11.8	25.09	4.30	-1	0.84	0.33	0.65	0.23	1.50	0.36	0.30	0.26	-	-
30	22:32:36.28	-60:36:16.1	24.50	4.42	-1	0.98	0.29	1.01	0.16	2.00	0.29	0.49	0.17	-	-
31	22:32:38.55	-60:36:29.0	25.33	4.16	-1	0.27	0.45	1.09	0.37	1.36	0.46	0.95	0.52	-	-
32	22:32:38.61	-60:34:13.4	25.27	1.99	-1	2.29	-1	0.77	0.30	3.06	-1	-0.00	0.30	-	-
33	22:32:40.05	-60:36:21.1	24.10	1.67	1.04	1.13	0.18	0.50	0.12	1.62	0.20	0.24	0.13	-	-
34	22:32:40.29	-60:35:25.4	25.86	2.36	-1	1.67	0.81	0.13	0.47	1.80	0.91	0.45	0.63	-	-
35	22:32:41.03	-60:34:04.6	25.79	-0.48	-1	3.69	-1	1.02	0.53	4.72	-1	0.12	0.51	-	-
36	22:32:42.19	-60:34:46.1	23.98	2.45	-1	1.13	-1	4.84	-1	5.97	-1	1.80	0.30	1.10	0.20
37	22:32:42.42	-60:35:49.3	25.59	2.26	-1	1.64	0.94	0.56	0.38	2.20	0.98	0.45	0.47	-	-
38	22:32:44.51	-60:33:12.6	25.51	1.69	1.24	0.46	0.22	0.00	0.30	0.46	0.33	-0.04	0.33	-	-
39	22:32:45.03	-60:34:56.1	25.70	1.81	-1	-0.04	0.43	0.68	0.51	0.64	0.50	0.04	0.49	-0.05	1.52
40	22:32:45.05	-60:31:27.6	25.65	-0.42	-1	3.66	-1	1.23	0.45	4.89	-1	-0.17	0.36	-	-
41	22:32:45.24	-60:35:05.1	25.11	4.18	-1	0.40	0.49	1.20	0.38	1.60	0.47	0.26	0.32	0.77	0.52
42	22:32:46.72	-60:32:10.7	25.93	2.64	-1	0.46	0.37	0.23	0.44	0.69	0.51	-0.21	0.46	-	-
43	22:32:46.99	-60:31:46.5	24.64	2.17	1.16	0.64	0.20	0.27	0.20	0.91	0.24	0.11	0.21	0.70	0.38
44	22:32:47.02	-60:36:02.5	25.67	2.14	-1	1.79	1.17	0.69	0.37	2.48	1.19	-0.08	0.37	-	-
45	22:32:47.49	-60:35:09.2	25.67	-3.14	-1	5.02	-1	1.11	0.59	6.12	-1	0.66	0.61	-2.87	-1
46	22:32:48.45	-60:32:37.3	25.02	6.07	-1	0.76	0.37	0.66	0.29	1.42	0.40	0.06	0.28	1.49	0.35
47	22:32:49.33	-60:32:25.3	23.44	1.52	0.30	0.46	0.09	0.20	0.09	0.65	0.10	0.02	0.09	0.40	0.20
48	22:32:49.97	-60:34:47.1	25.80	-0.10	-1	5.61	-1	0.38	0.52	5.99	-1	0.00	0.53	0.49	1.10
49	22:32:50.31	-60:31:27.0	25.64	-0.10	-1	5.24	-1	0.91	0.53	6.16	-1	0.58	0.57	1.43	0.57
50	22:32:51.05	-60:35:09.1	25.40	3.86	-1	1.11	0.45	0.52	0.29	1.62	0.49	0.16	0.32	-	-
51	22:32:52.07	-60:33:42.1	24.98	6.13	-1	0.73	0.33	0.56	0.28	1.29	0.36	0.11	0.27	1.00	0.42

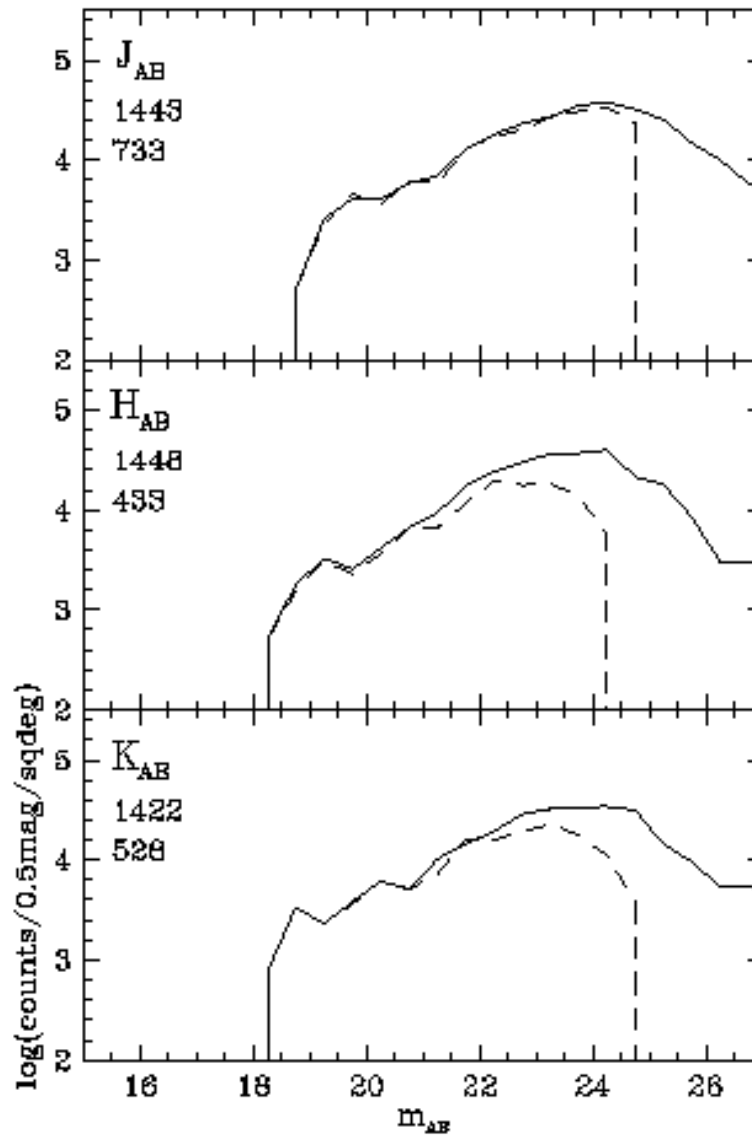
**Table 9.** High- $z$  Galaxy Candidates. Continued.

#	$\alpha$	$\delta$	$m_{ap}$	$(U-B)$	$\epsilon$	$(B-V)$	$\epsilon$	$(V-I)$	$\epsilon$	$(B-I)$	$\epsilon$	$(R-I)$	$\epsilon$	$(I-K)$	$\epsilon$
52	22:32:53.13	-60:32:06.2	24.36	2.01	-1	1.04	0.23	0.82	0.13	1.87	0.24	0.30	0.13	-	-
53	22:32:53.46	-60:35:24.5	24.46	4.85	-1	1.57	0.45	0.79	0.20	2.36	0.45	-0.01	0.18	1.23	0.26
54	22:32:53.48	-60:33:11.7	24.83	2.28	-1	0.40	0.27	0.69	0.25	1.08	0.30	0.47	0.28	1.22	0.34
55	22:32:53.62	-60:31:58.8	25.87	2.04	-1	1.53	1.26	0.77	0.46	2.30	1.28	-0.40	0.42	-	-
56	22:32:53.87	-60:35:41.1	25.93	5.76	-1	0.15	0.50	0.54	0.60	0.70	0.62	0.54	0.72	-2.62	-1
57	22:32:54.56	-60:33:23.9	26.02	2.09	-1	0.82	0.41	0.00	0.46	0.83	0.57	0.04	0.53	-	-
58	22:32:54.68	-60:34:30.6	24.69	4.17	-1	0.51	0.22	0.45	0.22	0.96	0.26	-0.02	0.21	0.92	0.35
59	22:32:55.34	-60:35:42.9	25.54	-2.50	-1	3.76	-1	1.34	0.42	5.10	-1	0.72	0.45	-	-
60	22:32:55.41	-60:33:54.5	23.85	0.22	-1	1.21	1.27	2.99	0.46	4.20	1.19	1.57	0.23	0.94	0.20
61	22:32:55.81	-60:32:51.6	26.18	4.23	-1	0.80	0.34	-0.38	0.52	0.43	0.59	-0.14	0.58	-	-
62	22:32:56.41	-60:31:43.8	25.55	6.49	-1	0.77	0.25	-0.42	0.38	0.35	0.42	-0.83	0.38	1.81	0.47
63	22:32:58.07	-60:34:55.8	25.90	-0.18	-1	3.38	-1	1.02	0.51	4.40	-1	0.76	0.64	-	-
64	22:32:58.46	-60:34:36.4	25.48	-0.10	-1	5.36	-1	0.96	0.47	6.31	-1	0.36	0.45	0.61	0.78
65	22:32:58.55	-60:31:58.4	25.88	3.67	-1	1.54	1.21	0.60	0.58	2.14	1.25	0.50	0.67	-2.67	-1
66	22:32:59.15	-60:35:07.6	25.50	-0.10	-1	4.89	-1	1.41	0.59	6.30	-1	0.88	0.59	1.50	0.50
67	22:32:59.21	-60:33:57.2	25.11	4.44	-1	0.07	0.38	1.06	0.36	1.13	0.37	0.94	0.43	2.05	0.31
68	22:33:02.49	-60:31:54.8	25.11	1.89	-1	-0.25	0.37	1.32	0.34	1.07	0.34	1.02	0.43	-	-
69	22:33:02.79	-60:33:32.4	25.90	-1.20	-1	2.28	-1	0.28	0.51	2.56	-1	-0.16	0.54	-	-

This figure "fig1.jpg" is available in "jpg" format from:

<http://arxiv.org/ps/astro-ph/9812105v1>





This figure "fig3.jpg" is available in "jpg" format from:

<http://arxiv.org/ps/astro-ph/9812105v1>

This figure "fig4.H.jpg" is available in "jpg" format from:

<http://arxiv.org/ps/astro-ph/9812105v1>

This figure "fig4.J.jpg" is available in "jpg" format from:

<http://arxiv.org/ps/astro-ph/9812105v1>

This figure "fig4.Ks.jpg" is available in "jpg" format from:

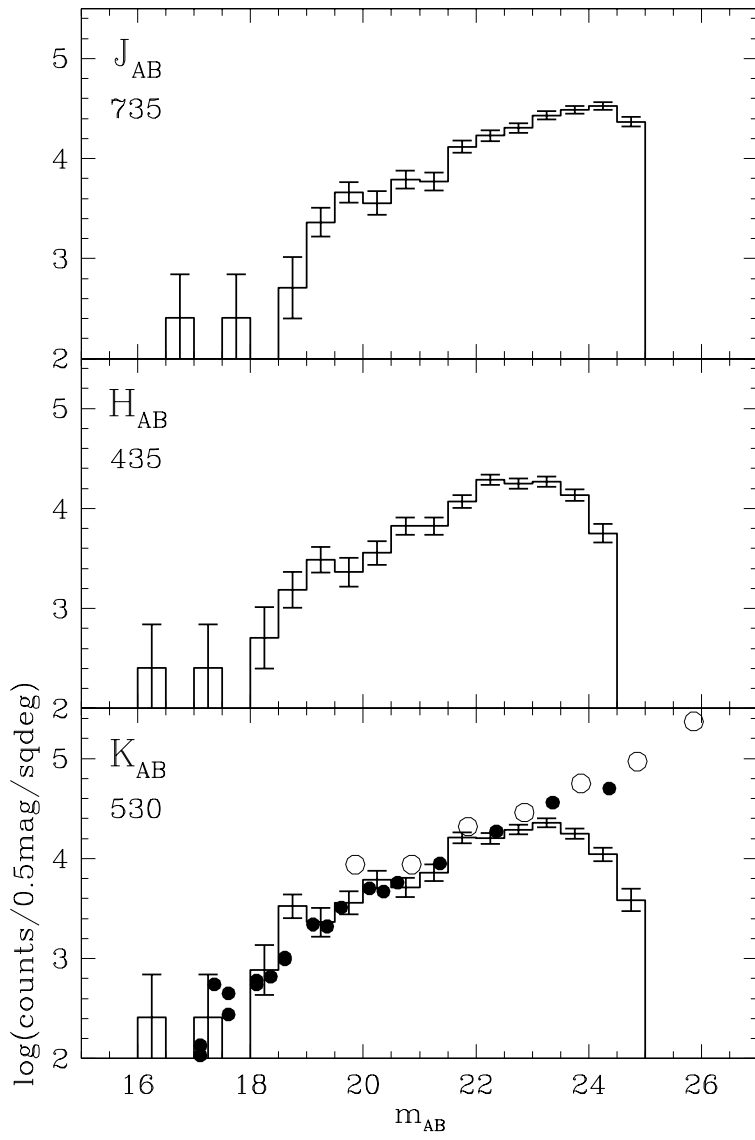
<http://arxiv.org/ps/astro-ph/9812105v1>

This figure "fig5.jpg" is available in "jpg" format from:

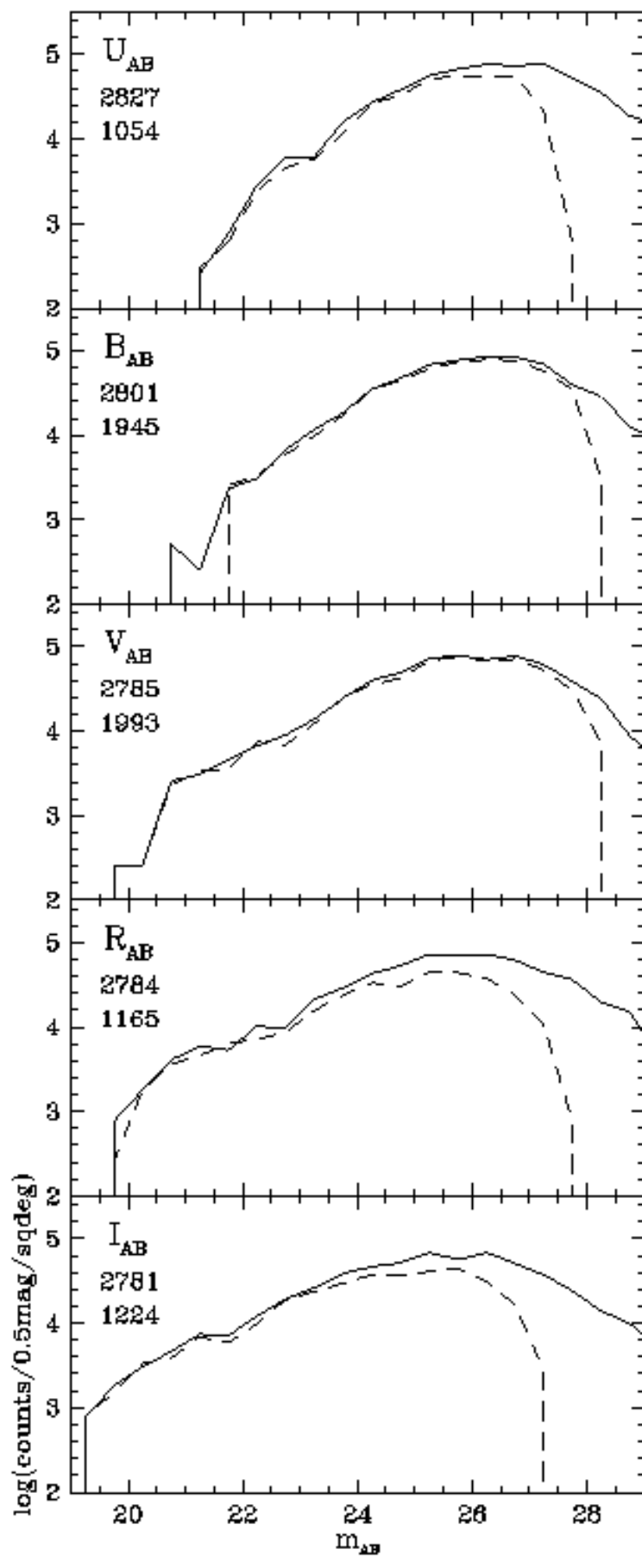
<http://arxiv.org/ps/astro-ph/9812105v1>

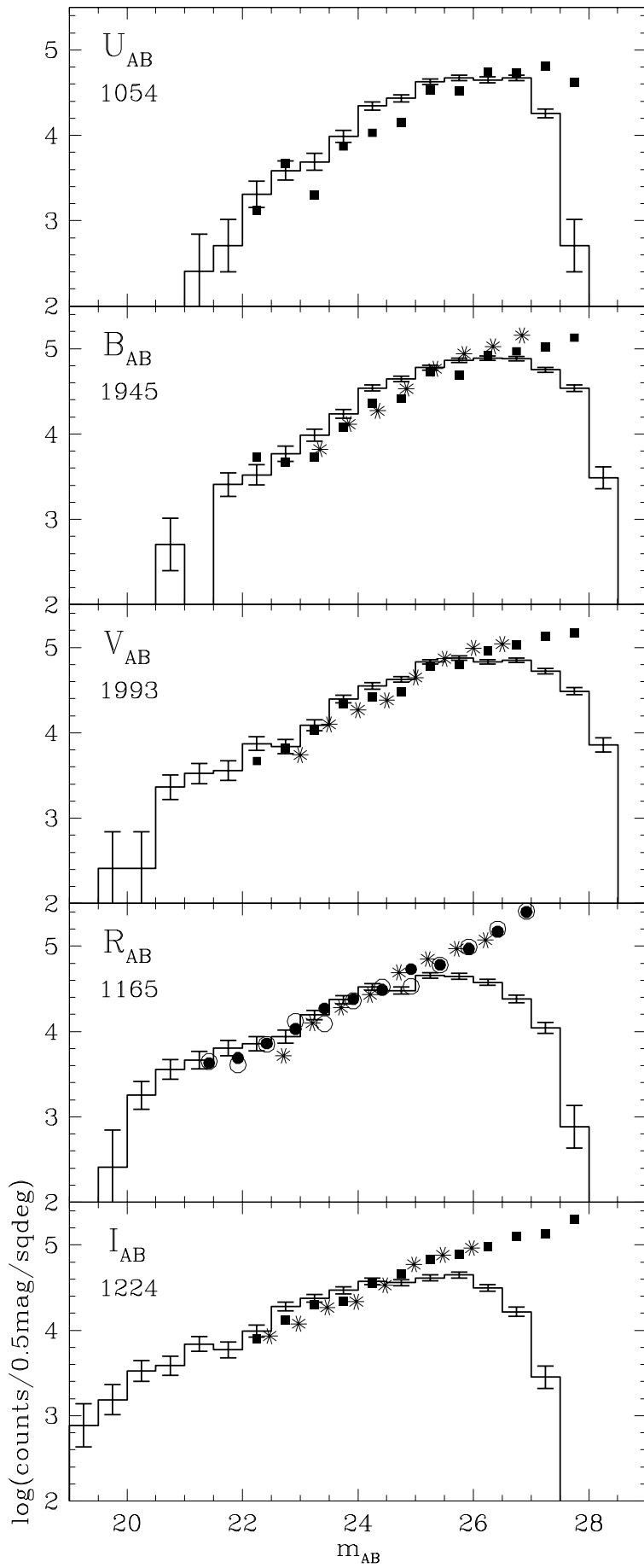
This figure "fig17.jpg" is available in "jpg" format from:

<http://arxiv.org/ps/astro-ph/9812105v1>









This figure "plate1.jpg" is available in "jpg" format from:

<http://arxiv.org/ps/astro-ph/9812105v1>

This figure "plate2.jpg" is available in "jpg" format from:

<http://arxiv.org/ps/astro-ph/9812105v1>